Bulletin of the
Seismological Society of America

Vol. 69 October 1979 No. 5

GENERALIZED RAY MODELS OF THE SAN FERNANDO EARTHQUAKE

By Thomas H. Heaton* and Donald V. Helmberger

ABSTRACT

The exact Cagniard-de Hoop solutions for a point dislocation in half-space are used to construct models of the strong ground motion observed during the February 9, 1971 San Fernando earthquake (M_L = 6.4). By summing point dislocations distributed over the fault plane, three-dimensional models of a finite fault located in a half-space are constructed to study the ground motions observed at JPL (Pasadena), Palmdale, Lake Hughes, and Pacoima Dam. Since the duration of faulting is comparable to the travel times for various wave types, very complex interference of these arrivals makes a detailed interpretation of these wave forms difficult. By investigating the motion due to small sections of the fault, it is possible to understand how various wave types interfere to produce the motion due to the total fault. Rayleigh waves as well as S to P head waves are shown to be important effects of the free surface. Near-field source effects are also quite dramatic. Strong directivity is required to explain the difference in amplitudes seen between stations to the north and stations to the south. Faulting appears to have begun north of Pacoima at a depth of 13 km. The rupture velocity, which is near 2.8 km/sec in the hypocentral region, appears to slow to 1.8 km/sec at a depth of 5 km. Displacements on the deeper sections of the fault are about 2.5 m. Fault offsets become very small at depths near 4 km and then grow again to 5 m near the surface rupture. The large velocity pulse seen at Pacoima is a far-field shear wave which is enhanced by directivity. Peak accelerations at Pacoima are probably associated with the large shallow faulting. The total moment is 1.4×10^{26} ergs.

Introduction

In this paper we present some preliminary results derived from strong motion modeling of some of the more diagnostic observations obtained from the San Fernando data set. In two related studies (Heaton and Helmberger, 1977, 1978), strong ground motions for several earthquakes located in the Imperial Valley were examined. The records in these situations were taken at distances several times larger than the source dimensions and only transversely polarized motions were modeled. Ground motions for these events were shown to be profoundly affected by seismic velocity structure. Although source characteristics were important, relatively simple source models were all that were necessary to produce adequate synthetic records. This study attempts to understand recordings of the 1971 San Fernando earthquake. Since this earthquake was well recorded by many close stations, a more detailed inspection of source processes is required.

* Present address: Dames & Moore, Suite 1000, 1100 Glendon Avenue, Los Angeles, California 90024.

Several new complications are introduced by the small source-to-receiver distances. Near-field terms can no longer be neglected as in the previous studies. Furthermore, fault finiteness requires that waves from differing parts of the fault must approach the receiver from differing directions. This means that the observed ground motion cannot be rotated into radial and transverse directions. Thus we cannot isolate *SH* wave forms and we are forced to consider *P* waves, *SV* waves, and Rayleigh waves. For many reasons, life becomes more complicated as we move closer to the earthquake source. Fortunately, as the source-to-receiver distance becomes small, the effects of plane-layered structure become less dramatic. In an attempt to understand the most basic features of the interplay between source and structural effects, we chose first to model the San Fernando earthquake as a three-dimensional fault located in an elastic half-space.

The purpose of this study is two-fold. We would first like to understand the types of phenomena which should be expected from a three-dimensional fault which is located in a half-space. The second goal is to achieve a better understanding of the particular source processes of the San Fernando earthquake. The second goal is the more important and difficult to achieve. The San Fernando earthquake created a wealth of teleseismic body-wave and surface-wave data and also local static offset data. It thus provides a unique cross-check of several different techniques of studying the slip on the fault plane. Ultimately, we would like to find a single model which explains all of these observations. However, in this study we will not attempt to model these different data sets simultaneously. We will comment on the compatibility of our strong-motion models which have been derived by other authors.

A large number of papers have been written about the San Fernando earthquake and we will not attempt to summarize the results of all previous studies. However, these are several papers which we found very useful in constructing our models. The study of teleseismic body waves by Langston (1978), Alewine's (1974) inversion of static offset data and teleseismic surface-wave data, Hanks' study of observed strong ground motion (1975), and the inversion of strong-motion data by Trifunac (1974) all proved very useful in our construction of San Fernando models. Although Trifunac's models were for a finite fault in a whole space, we learned from his synthetic Pacoima Dam ground motion. Thus, there are several similarities between our preferred fault model and Trifunac's final fault model.

The numerical calculations involved in our synthetics consist of several relatively laborious and expensive steps. Once a particular fault to station geometry is chosen, it is time and money consuming to change that geometry. We have chosen to model four stations and no attempt was made to find alternate stations or source-to-station geometries which might produce better synthetics. In retrospect, we would have ignored the station at Palmdale since a half-space seems to be a very poor approximation of earth structure near this station. Also, it appears that a different fault dip versus depth relationship might have improved the comparison between synthetic and real data. However, it is not our purpose to discover the best half-space model. We would like to discover the gross features of the model which are required by the data. Because of the large number of parameters involved, a thorough search of the model space can result in an endless groping process. Until we learned the significance of different parameters, we were victims of this grope. The merits of this process are that much can be learned about what will not work.

We are now faced with the problem of showing the reader what we have learned from this process and why we have chosen the model presented in this paper. It would be impractical and tedious to present all of our unsuccessful models. Thus

our plan is to present several simple models and to then try and understand why they do not work and how they could be improved.

The Data

The 1971 San Fernando earthquake produced by far the largest single strong-motion data set yet available. Shown in Figure 1 are the locations of most of the

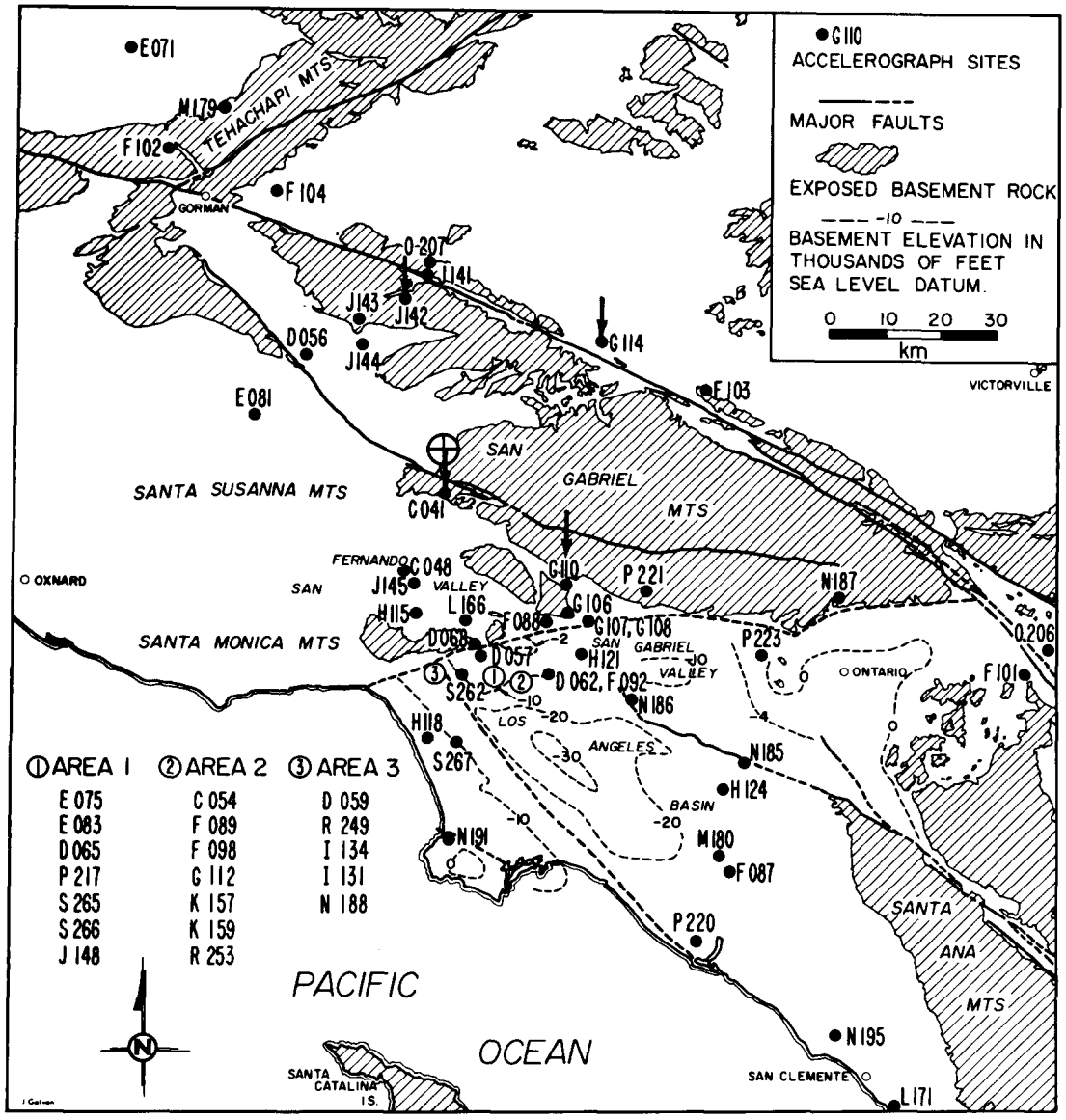

FIG. 1. The site locations of accelerometer recordings of the San Fernando earthquake are superimposed on the gross geological and structural features of the area. The encircled cross is the Allen *et al.* (1973) epicenter and the arrows point to stations which are studied in this paper (modified from Hanks, 1975).

accelerometers which recorded this event. We were faced with the choice of which records from this immense set we would model. Because we are using a half-space model, it is important that the stations be near the fault. In order to minimize redundant information, stations from different azimuths were chosen. The stations

for which records were synthesized are Pacoima Dam (PAC), Jet Propulsion Laboratory (JPL), Lake Hughes Array Station 4 (LKH), and Palmdale Fire station (PLM). These stations are indicated in Figure 1 by the codes C041, G110, J142, and G114, respectively. These codes refer to the cataloging system used in the series of strong-motion data reports published by the Earthquake Engineering Research Laboratory of the California Institute of Technology. It is from these reports that our observed ground displacement curves have been taken. In Figure 2 through 5 we show the corrected accelerograms, integrated ground velocity, and displacement curves for these stations (Trifunac *et al.*, 1973b). The processing of these accelerograms involves base line corrections and Ormsby filtering. The basis for this processing can be found in papers by Trifunac (1971) and Trifunac *et al.* (1973, a and b).

It is impossible for an accelerometer to recover static or even very long-period ground displacement information and thus these integrated displacement curves are really displacements in which periods longer than 10 sec have been heavily filtered. In fact, the base line correction can effectively filter periods of less than 10 sec. For instance, the Pacoima station probably experienced a large static offset which cannot be easily seen when simply viewing the displacement curves. Hanks (1975) has presented a relatively comprehensive discussion of the sources of long-period errors for this data set.

In his 1975 paper, Hanks also investigates the coherence of displacements between stations which are located near each other. In general, he finds this coherence to be very good. In particular, the records from stations in the Pasadena area (i.e., JPL) are very similar to each other. The same is true of records obtained in the Lake Hughes area. Unfortunately, there are only two stations to the northeast, Palmdale and Pearblossom. We chose Palmdale since it was closest.

Hanks (1975) points out that both the intensity of shaking and amplitude of displacements were generally larger for regions south of the hypocenter. In particular, this is true of the stations which we have chosen to model. We will use these observations to try and pin down the slip on the fault plane.

The Model

Our model consists of a three-dimensional finite fault located in a half-space. A circular rupture front is assumed to propagate at a given rupture velocity from the hypocenter. The slip angle and dislocation time history are assumed to be uniform throughout the fault plane. The Cagniard-de Hoop technique, together with a linear interpolation scheme, is used to compute the ground motions from point dislocations which are evenly distributed (0.5 km spacing) on the fault plane. These responses are summed with time lags which are determined by the assumed hypocentral solution and rupture velocity. Nonuniform fault displacement is modeled by varying the weights of individual point sources. We are thus using a numerical Green's function technique to integrate over the fault plane. This is very similar to the finite fault models which were constructed for the Borrego Mountain earthquake in our 1977 paper. However, unlike the Borrego study in which we considered only *SH* motions, there are many added complexities due to the inclusion of *P* and *SV* waves, near-field terms, and a more general fault-to-station geometry which dictates that waves arrive from different azimuths. This last complication has two effects, both of which are included, without approximation, in our models. The first effect originates from the fact that sources having different locations on the fault plane have different radiation patterns with respect to a fixed station. The second effect is to make the

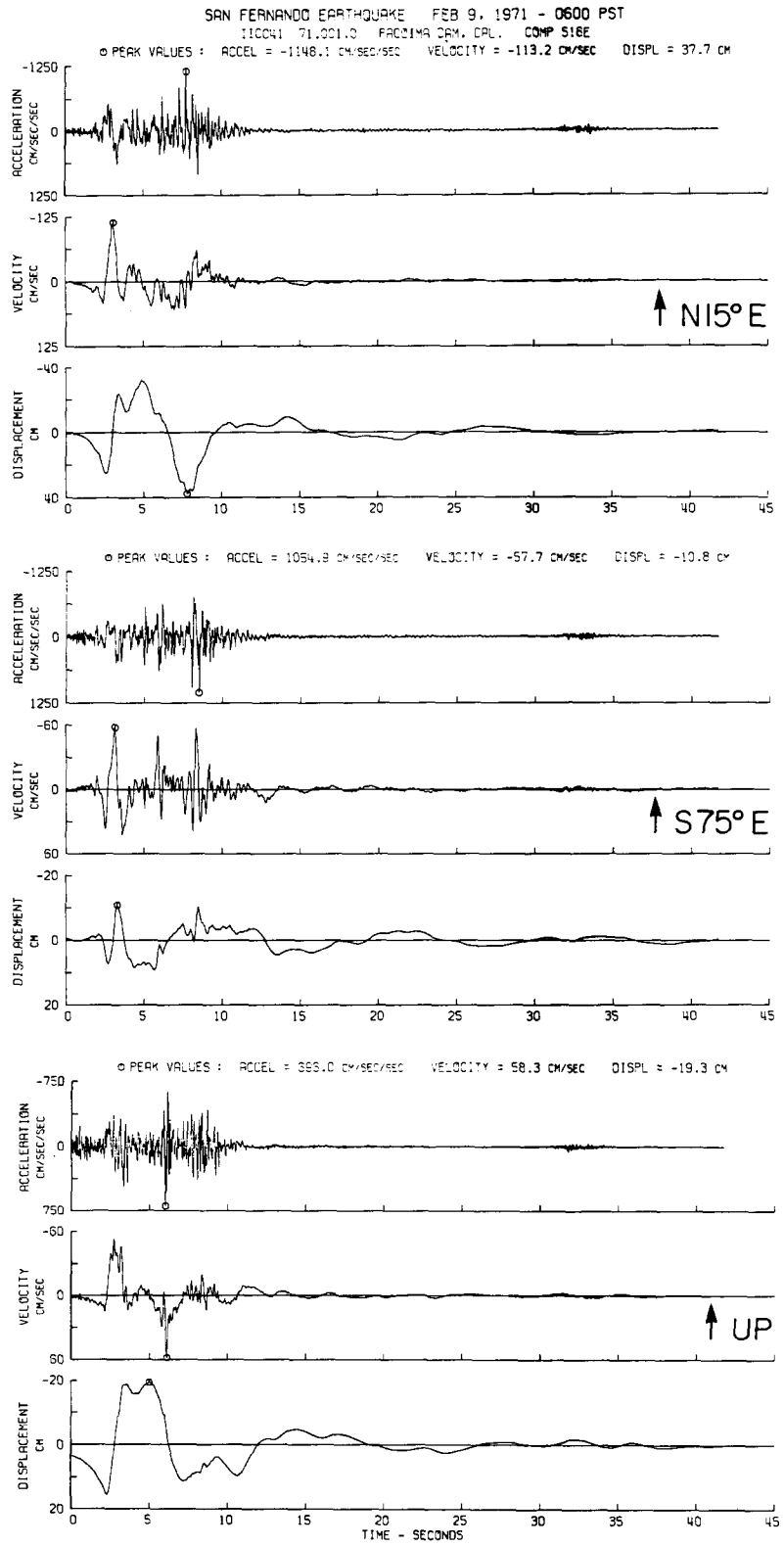

FIG. 2. Corrected accelerograms, velocities, and displacements for the San Fernando earthquake as recorded at Pacoima Dam (modified from Trifunac *et al.*, 1973b).

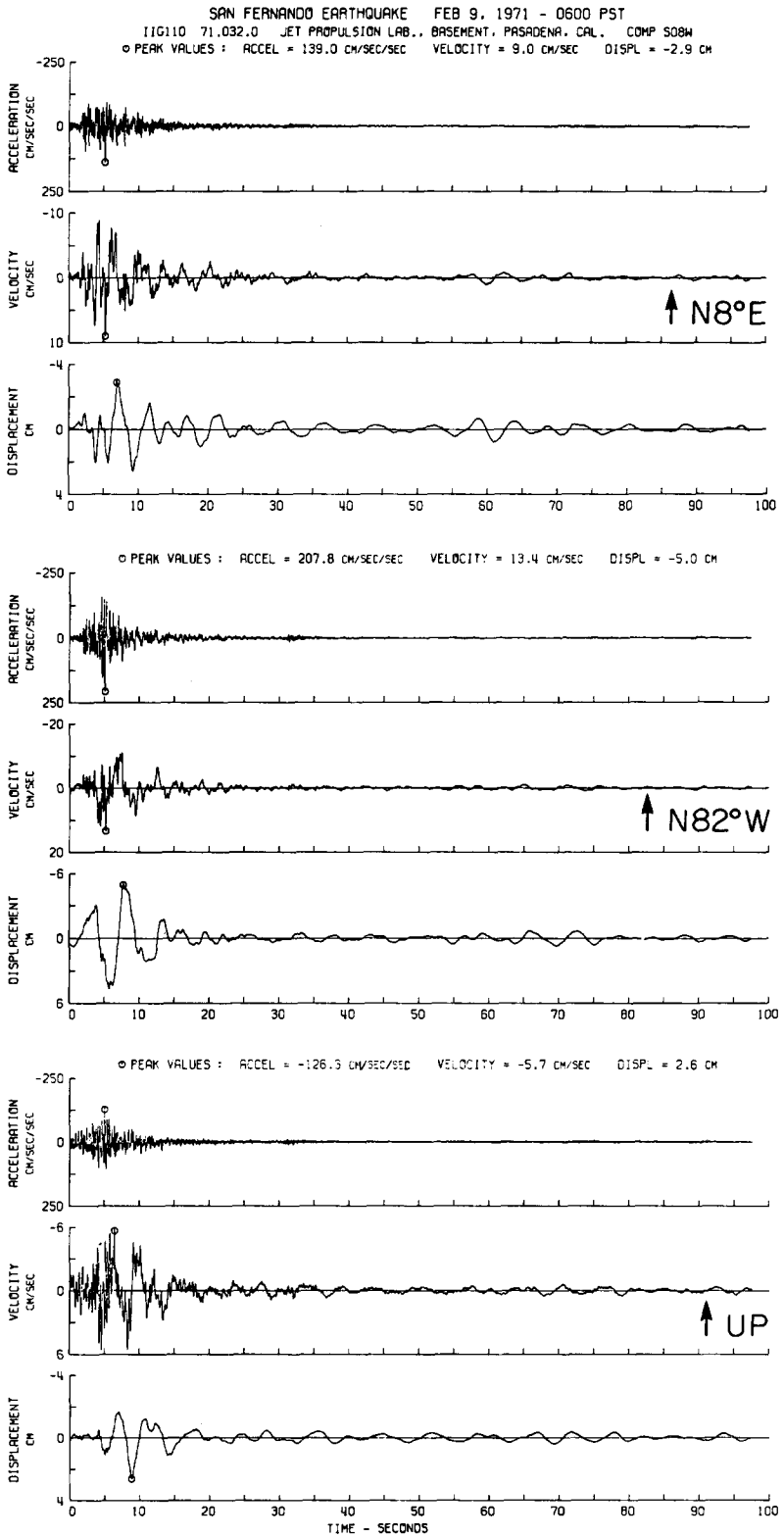

FIG. 3. Corrected accelerograms, velocities, and displacements for the San Fernando earthquake as recorded at the Jet Propulsion Laboratory (modified from Trifunac *et al.*, 1973b).

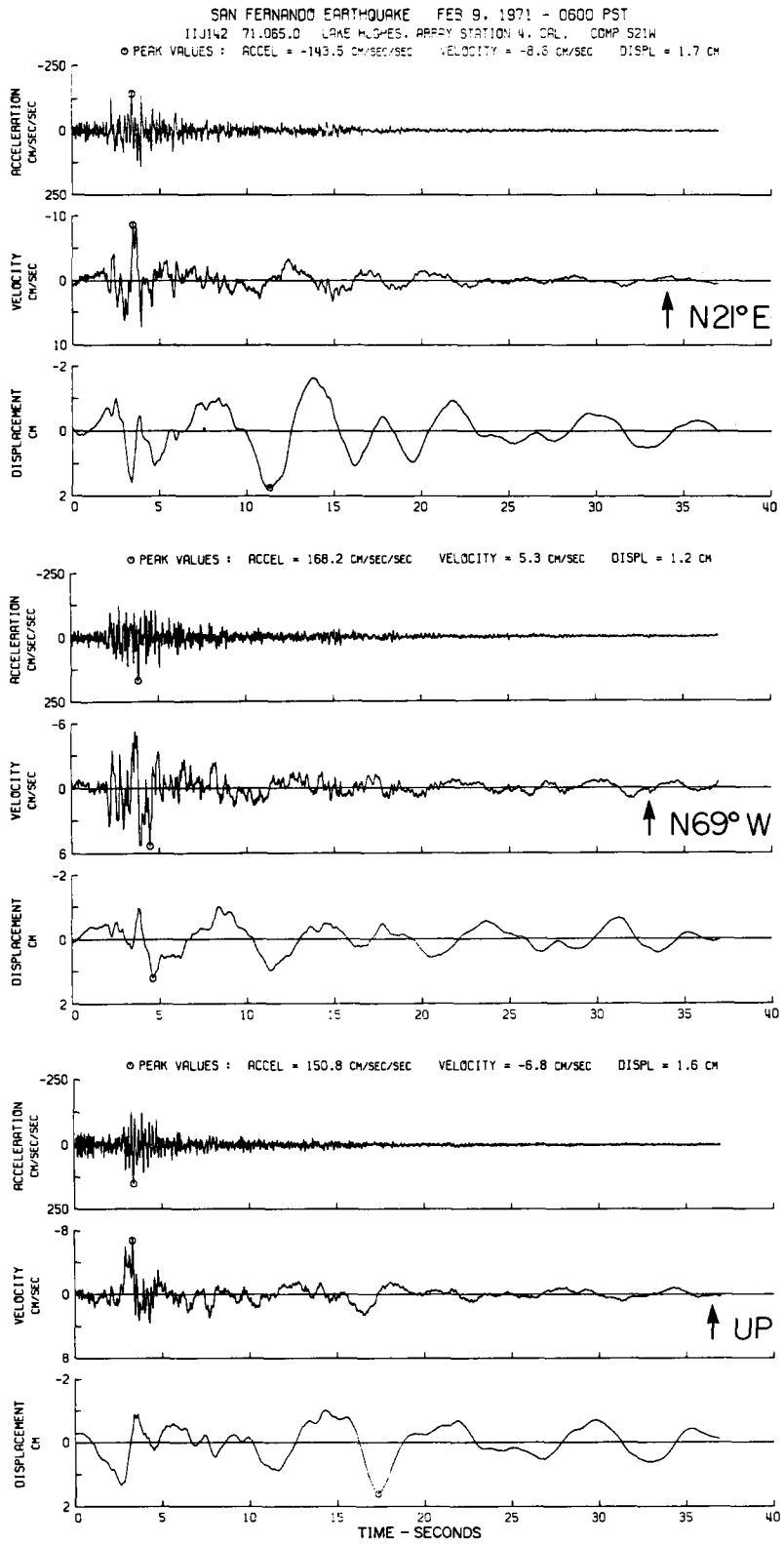

FIG. 4. Corrected accelerograms, velocities, and displacements for the San Fernando earthquake as recorded at the Lake Hughes array station 4 (modified from Trifunac *et al.*, 1973b).

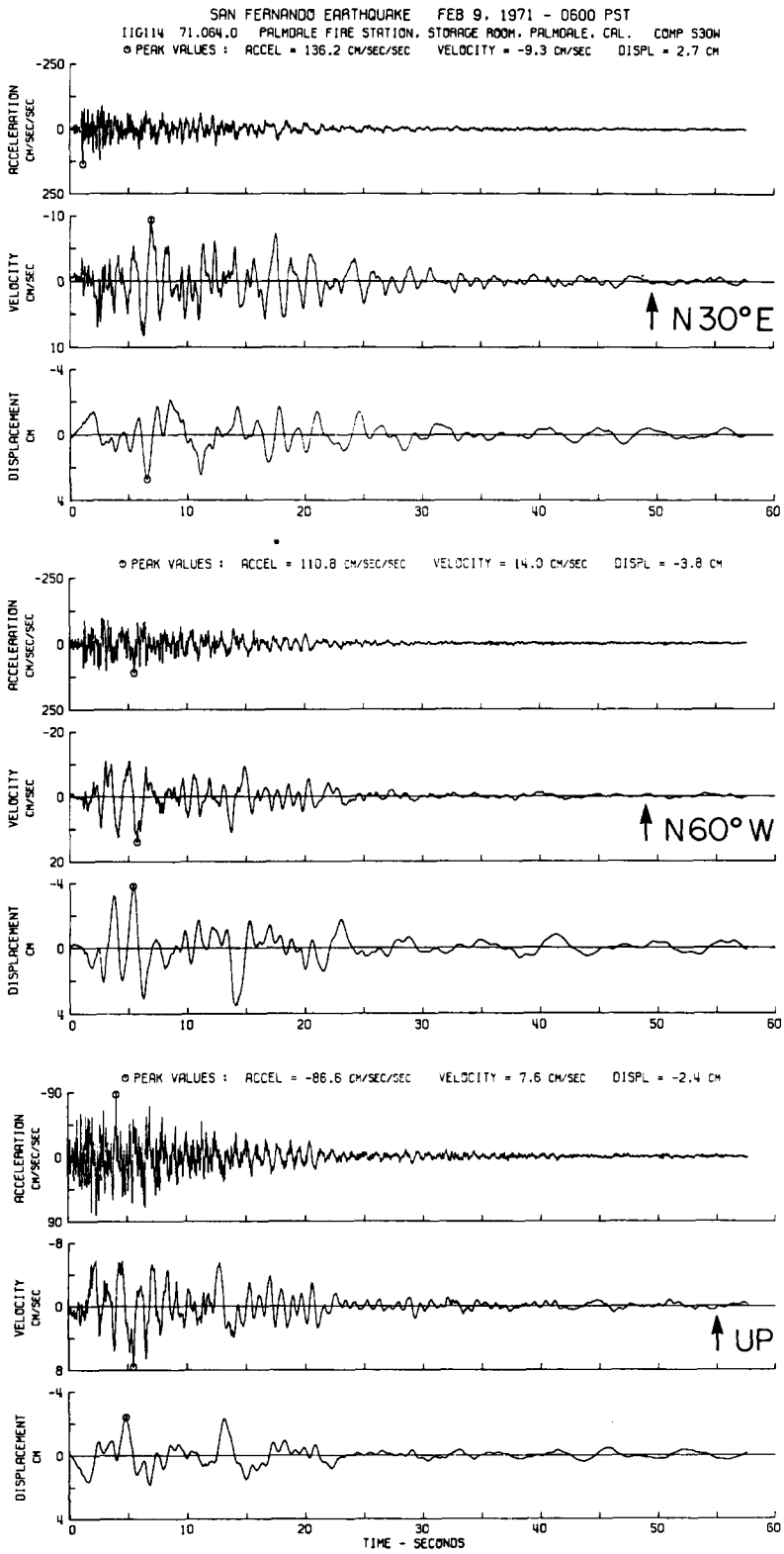

FIG. 5. Corrected accelerograms, velocities, and displacements for the San Fernando earthquake as recorded at the Palmdale Fire station (modified from Trifunac *et al.*, 1973b).

definition of radial and transverse directions a function of the position of the point on the fault being considered at any one time. The importance of these effects is a function of the source dimensions and the receiver distance, and they are particularly important in the Pacoima models.

Our total solution can be formally written as

$$\mathbf{U}(t) = \sum_{j=1}^{n} \sum_{k=1}^{m} m_{jk} \mathbf{Y}_{jk}(t) * \dot{D}(t), \tag{1}$$

where $\mathbf{U}(t)$ is the displacement at a station, j denotes the jth source along the fault strike, k denotes the kth source down the fault dip, m_{jk} is the moment and $\mathbf{Y}_{jk}(t)$ is the response of the j, kth source, and $\dot{D}(t)$ is the time derivative of the time history for any point on the fault which we assume to be uniform at this stage. If we choose the coordinate frame ($\mathbf{e}_1$, $\mathbf{e}_2$, $\mathbf{e}_3$) to be north, east, and down, then

$$\mathbf{Y}_{jk}(t) = (Q_{jk} \cos \nu_{jk} - V_{jk} \sin \nu_{jk})\mathbf{e}_1 + (Q_{jk} \sin \nu_{jk} + V_{jk} \cos \nu_{jk})\mathbf{e}_2 + W_{jk}\mathbf{e}_3, \tag{2}$$

where we have used the notation

$$\begin{aligned} Q_{jk} &= Q(r_{jk}, h_{jk}, \theta_{jk}, \lambda, \tau) \\ V_{jk} &= V(r_{jk}, h_{jk}, \theta_{jk}, \lambda, \tau) \\ W_{jk} &= W(r_{jk}, h_{jk}, \theta_{jk}, \lambda, \tau) \end{aligned} \tag{3}$$

and where r_{jk} is the distance of the j, kth source, h_{jk} is its depth, θ_{jk} is its azimuth angle as defined from the fault strike, λ is the rake, and ν_{jk} is the backazimuth angle of the j, kth point source as measured clockwise from north. Q, V, and W are the radial, transverse, and vertical components of motion, respectively, as discussed in Helmberger and Harkrider (1978) and in detail by Heaton (1978).

We begin by constructing a coarse gridwork on the fault. Responses for points located on the corners of this gridwork are computed by using the exact Cagniard solutions. These solutions are extremely broad band; that is, they are correct for the static as well as the very high-frequency parts of the solution. If the gridwork spacing is small enough, then responses from adjacent sources look very similar. It is thus possible to calculate other responses on a finer gridwork by interpolation. Our scheme is as follows. Responses from adjacent points are shifted in time such that their direct shear-wave arrival times coincide. Then a simple linear interpolation is used to calculate the shape of the approximate solution for intermediate locations. The approximate solution is again shifted in time such that the shear wave arrival time for the approximate solution is exactly correct. Hartzell *et al.* (1978) have also devised a similar method for approximating intermediate point source responses.

The accuracy of the interpolated solutions is a function of frequency and the distance between coarse grid points. The solutions are very good at the longer periods which dominate the displacement records. Because the interpolation is based on shear-wave arrival times, the approximation for the direct shear is quite good for all frequencies. However, the high-frequency parts of the solution for phases with different phase velocities than the direct shear wave are poorly approximated by this scheme. For instance, the direct compressional wave will appear as two sharp arrivals instead of just one. This is not a great worry to us, however, since

the largest high-frequency arrival is the direct shear wave and also because our synthetic displacements are rather insensitive to the details of the high frequency anyway.

For stations except Pacoima, exact responses were computed every 4 km along the strike and every 2 km down the dip. Since Pacoima is so close to the fault, this spacing was halved for Pacoima. Interpolated responses were calculated at a 0.5 km spacing.

It is interesting to note that our interpolation technique could be replaced with a convolution technique such as the one employed by Wiggins *et al.* (1978). That is, instead of summing interpolated sources, we could sum only the coarse grid where each source would be convolved with a separate time function which would approximate the finiteness of that section of the fault. We can demonstrate this equivalence by considering one element of the gridwork on the fault. Consider the fault element shown in Figure 6, for which exact responses have been computed at the corners.

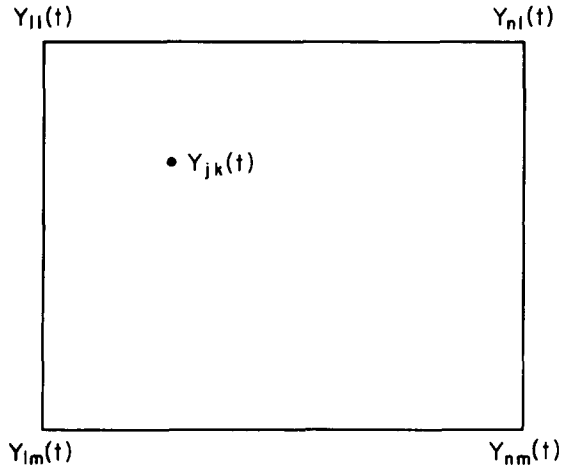

FIG. 6. Schematic of one subdivision of a finite fault. Exact responses are computed at the corners and responses within the subdivision are then computed by linear interpolation.

For simplicity, consider this to be a scalar problem with the scalar displacement u; u is given by

$$u = \sum_{j=1}^{n} \sum_{k=1}^{m} Y_{jk}(t). \tag{4}$$

Now our linear interpolation technique says that the j, kth response can be approximated by

$$Y_{jk} = a_{jk}^{11} Y_{11}(t - \tau_{ij}^{11}) + a_{jk}^{11} Y_{n1}(t - \tau_{ij}^{n1}) + a_{jk}^{1m} Y_{1m}(t - \tau_{ij}^{1m}) + a_{jk}^{nm} Y_{nm}(t - \tau_{ij}^{nm}), \tag{5}$$

where the a_{jk}^{nm} are interpolated constants, and the τ_{ij}^{nm} are time shifts which are used to ensure that shear-wave arrival times are aligned during interpolation. These time lags may also contain information about the rupture process. Noting that

$$Y_{11}(t - \tau_{ij}^{11}) = Y_{11}(t) * \delta(t - \tau_{ij}^{11}),$$

we can write equation (4) as

$$u = Y_{11}(t)*A_{11}(t) + Y_{n1}(t)*A_{n1}(t) + Y_{1m}(t)*A_{1m}(t) + Y_{nm}(t)*A_{nm}(t), \quad (6)$$

where

$$A_{il}(t) \equiv \sum_{j=1}^{n} \sum_{k=1}^{m} a_{jk}^{il} \delta(t - \tau_{jk}^{il}).$$

Thus we see that our interpolation scheme is a way of finding the appropriate far-field time functions for point sources located on our coarse gridwork. In our actual models, the interpolation technique includes the second order effects due to the

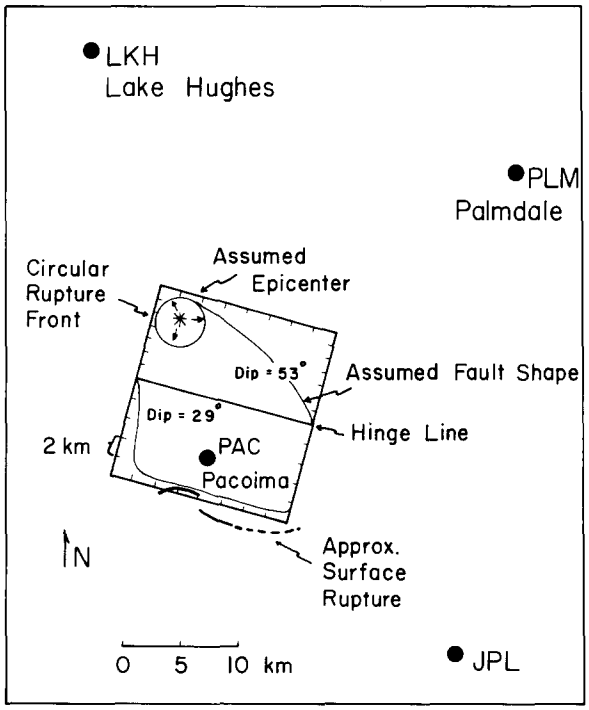

FIG. 7. Assumed geometry for the San Fernando fault and receivers. Model consists of a three-dimensional fault in a half-space. A circular rupture front propagates from an assumed hypocenter and displacement magnitudes are prescribed on the fault surface. Notice that the fault changes dip at a depth of 5 km.

variation in azimuth angle between individual point sources and the receiver. These variations cannot be included in a convolution technique, but as long as the spacing of the coarse gridwork does not become too large, these azimuthal effects are very small. Finally, it is important to realize that both the interpolation and convolution techniques may poorly approximate the high-frequency behavior of phases other than the direct shear wave. As we have said before, this is not a severe problem for the half-space solution. However, some care should be taken when applying these techniques to a layered half-space problem, since there may be several other important high-frequency phases present.

In Figure 7 we show the fault and station geometry that was used in this study. Unfortunately, picking a fault geometry is largely guesswork. Allen *et al.* (1973) have

argued that the fault dip increases with depth. They based this result on the discrepancy between the aftershock pattern and the teleseismic focal mechanism. Langston (1978) has concluded that the wave forms of teleseismic body waves require a depth-dependent dip. He found that he could adequately synthesize the teleseismic wave forms with a hinged fault in which the strike, dip, and rake of the upper and lower planes are (Θ_1 = N80°W, δ_1 = 29°, λ_1 = 90°) and (Θ_2 = N70°W, δ_2 = 53°, λ_2 = 76°), respectively. These two faults intersect at a depth of 5 km. We have incorporated these two planes in our solution. However, for the sake of simplicity, we have assumed that $\Theta_1 = \Theta_2$ = N75°W. Thus, the fault geometry used in this study was chosen independently of the strong-motion modeling results.

Modeling the Records

Our basic objective is to search through a model space in which the hypocentral solution, rupture velocity, and distribution of faulting are allowed to vary. We would like to discover which models adequately explain the records we have chosen to model. Our model space is large and it is unreasonable for us to randomly search through it. Thus, it is important that we learn from the small number of models which we have the time to study. Langston (1978) and Hanks (1974) have both argued that the timing of the teleseismic *pP* phase indicates a hypocentral depth of 13 km. Hanks suggests that the hypocenter is located 13 km due north of Pacoima. A recent relocation by Hadley and Kanamori (1978) indicates that the hypocenter is several kilometers south of Hanks' solution at a depth of 11.5 km. Langston found that a bilateral rupture on a uniform fault with a width of 10 km and upward and downward rupture velocities of 1.8 km/sec and 3/0 km/sec yielded a good fit to the teleseismic body waves. He also concluded that the moments of the upper and lower fault segments were 0.41×10^{26} ergs and 0.45×10^{26} ergs, respectively. In Figure 8 we show a model similar to Langston's except that we have omitted the small lower section that supposedly propagated downward with a high rupture velocity. We will return to the rather undesirable effects produced by this feature later. The contours in Figure 8 signify lines of equal fault slip in meters. The hypocenter is located in the region of maximum slip and the rupture velocity is 1.8 km/sec. The time derivative of the time history of slip for each point on the fault is an isosceles triangle with a duration of 0.8 sec. The fault moment, 1.5×10^{26} ergs, is significantly larger than Langston's moment.

Comparisons of synthetic and observed records for the model we designated Norma 140 are also shown in Figure 8. Two synthetic records are shown for each component. The *top trace* is the computed ground motion and the *middle trace* is this synthetic motion with a base line correction and a high-pass Ormsby filter applied. We used the base line correction described by Nigam and Jennings (1968) and an 8-sec Ormsby filter. This filter is described by Hanks (1975).

The first thing that we notice about Norma 140 is that, although relative amplitudes are approximately correct, the synthetic wave forms are quite dissimilar from the observed. First inspect the synthetics from Pacoima. Notice that the static part of the solution can be very important and also notice that the filtering process can severely alter the shape of the records. The observed record begins with a sharp pulse which is not seen on the synthetics. The polarity and timing of this pulse are that which is expected for a far-field *SV* wave originating from the hypocentral region. Hanks (1974) has argued that this pulse requires energetic but localized faulting in the hypocentral region. Norma 140 does not refute this argument since the fault model is smooth and the pulse is absent. The later parts of these synthetics also fit poorly and, for the moment, we will leave this unexplained.

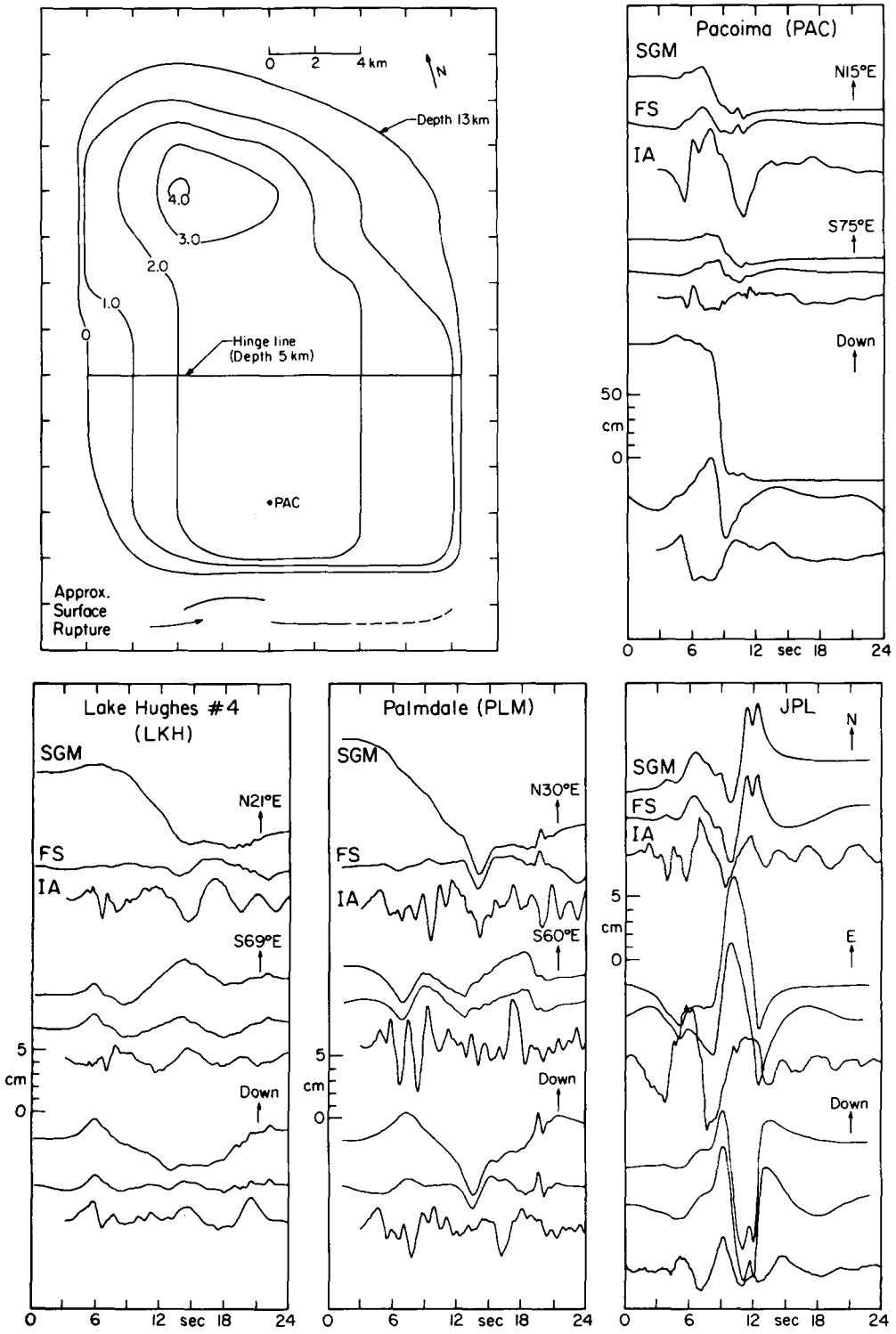

FIG. 8. Summary of the model Norma 140. A contour map of assumed dislocation (in meters) is shown in the upper left. The rupture velocity is 1.8 km/sec and the hypocenter is near the region of maximum displacement. Also shown are the comparisons of observed and synthetic displacements for the four stations, PAC, JPL, LKH, and PLM. The top trace is the synthetic ground motion (SGM); the middle trace is the synthetic ground motion after base line correction and Ormsby filtering (FS); the bottom trace is the observed displacement which has also been filtered and base line corrected (IA).

Next, we consider the JPL records. Notice that the observed east record begins with a large pulse which cannot be found in the synthetic record. The comparison of the later parts of the records is more favorable even though the amplitudes of the synthetics are too large. The synthetic fit to the records at Lake Hughes looks promising, although several short-period arrivals which are present in the observed records are absent from the synthetics. Also, the later parts of the observed records contain larger and shorter period waves than do the synthetics. Finally, notice poor correlation between observed and synthetic Palmdale records. The observed records are dominated by a "ringing" at 1 Hz which cannot be found in the synthetics.

In general, Norma 140 is, at best, a marginally successful attempt to explain the observed records. How might we improve this model? Perhaps massive faulting in the hypocentral region (the hypothesis proposed by Hanks, 1975) will help to make the large first pulses seen at Pacoima and JPL. In Figure 9 we show the slip contour map for the model, Norma 170. This model is very similar to Norma 140, except that displacements of up to 12 m are present in the hypocentral region. Once again the total moment is 1.5×10^{26} ergs with the upper and lower faults contributing equally to this total. The rupture velocity is still 1.8 km/sec.

The comparisons between synthetic and observed records for model Norma 170 are also shown in Figure 9. A quick glimpse at these comparisons shows that the hoped for miracle has not yet occurred. The first pulse on the Pacoima and JPL records has grown significantly. Unfortunately, it is still less than half the amplitude of the observed. How might we increase the amplitude of this pulse? We could either further increase the displacements, or we could increase the rupture velocity. Either of these alternatives looks promising until we study the Lake Hughes synthetics. When we increased the first pulse for PAC and JPL, we also increased it for LKH. The trouble is that this synthetic pulse is now too large at LKH. We are in a dilemma. How can we make the first pulse large at JPL and PAC, and yet still keep it small at LKH and PLM? As you may have already guessed, directivity is our way out.

Before we get to the details of the lower fault, it is instructive to study the model Norma 170 with greater care. Remember that we also have to find some way to improve the later part of the synthetics, particularly for the Pacoima records. Figures 10 through 13 show how the synthetics for Norma 170 were constructed. These figures may seem complicated and tedious, but a careful study of them is very rewarding. Each picture corresponds to one synthetic record. On the left, the fault is subdivided into the five strips designated A through E. The responses of each of these strips are shown and their sums, the synthetics for Norma 170, are shown at the bottom. This allows us to associate arrivals in the synthetics with particular parts of the fault. The middle and right hand columns contain the responses of point dislocations which are convolved with the far-field time functions shown. The durations of these time functions are 0.8 and 3.0 sec. The locations of these sources are shown to be in the middle of the various strips. The peak amplitudes of these point sources are shown next to each trace. This amplitude, given in centimeters; corresponds to a point source whose moment is $\pi \times 10^{26}$ ergs.

Notice that there is usually an excellent correspondence between the responses of the fault strips and the point responses which have been convolved with the 3.0-sec time functions. Furthermore, it is fairly easy to identify individual arrivals on the short-period point responses, which in turn allows us to identify arrivals on the long-period responses and on the responses of the fault strips.

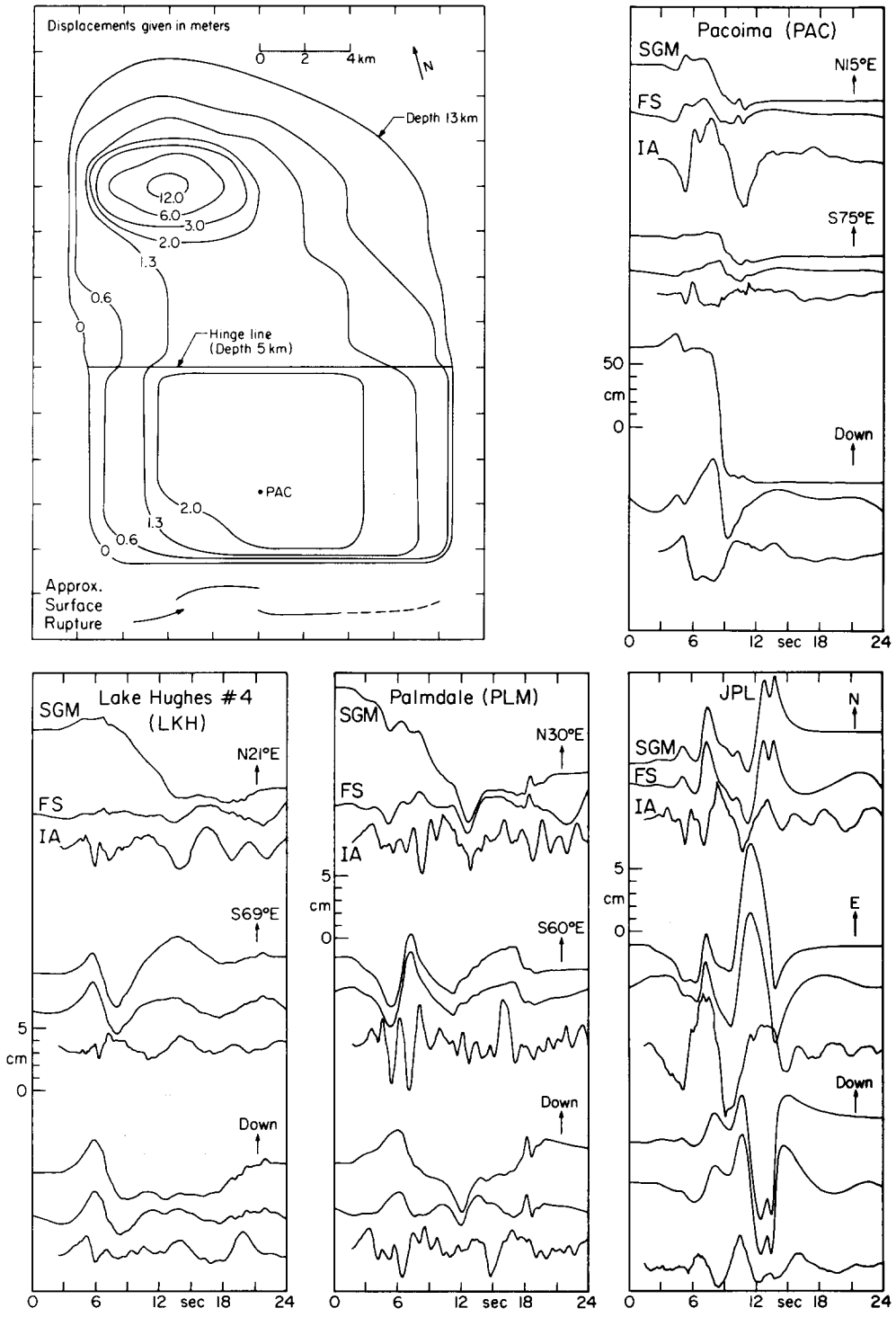

FIG. 9. Summary of the model Norma 170. The rupture velocity is 1.8 km/sec and the hypocenter is near the region of maximum dislocation. See Figure 8 for a more detailed figure explanation.

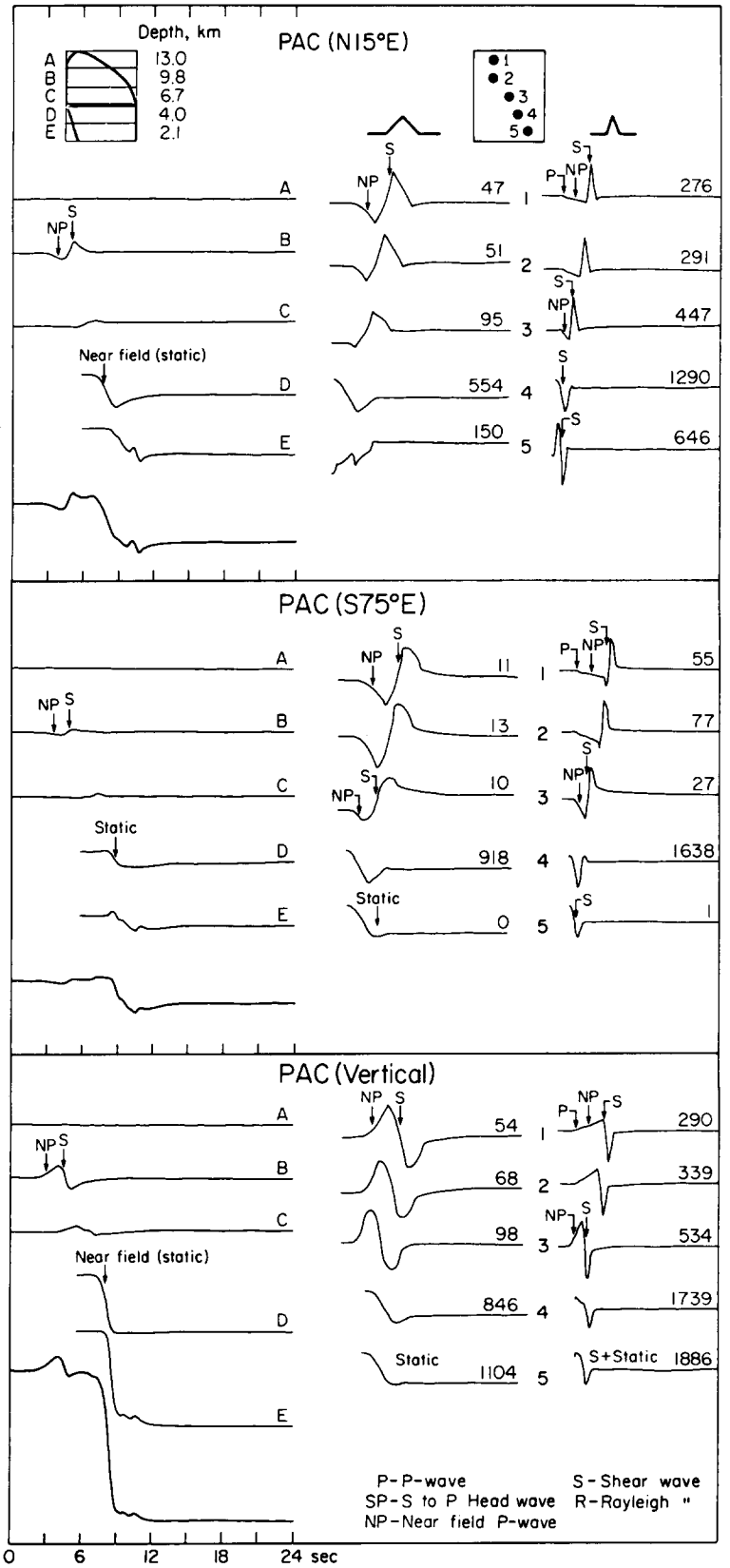

FIG. 10. Decomposition of the synthetic ground motions for PAC and the model Norma 170. The finite fault is broken into five strips whose individual contributions are shown on the left. Responses of point sources which lie in these strips have been convolved with both 3 sec and 0.8 sec triangular far-field time functions and are displayed in the *middle* and on the *right*, respectively. The numbers signify peak displacements in centimeters for point sources having moments of $\pi \times 10^{26}$ ergs. By studying the point-source responses, contributions of individual phases can be recognized in the synthetic motion from the finite fault.

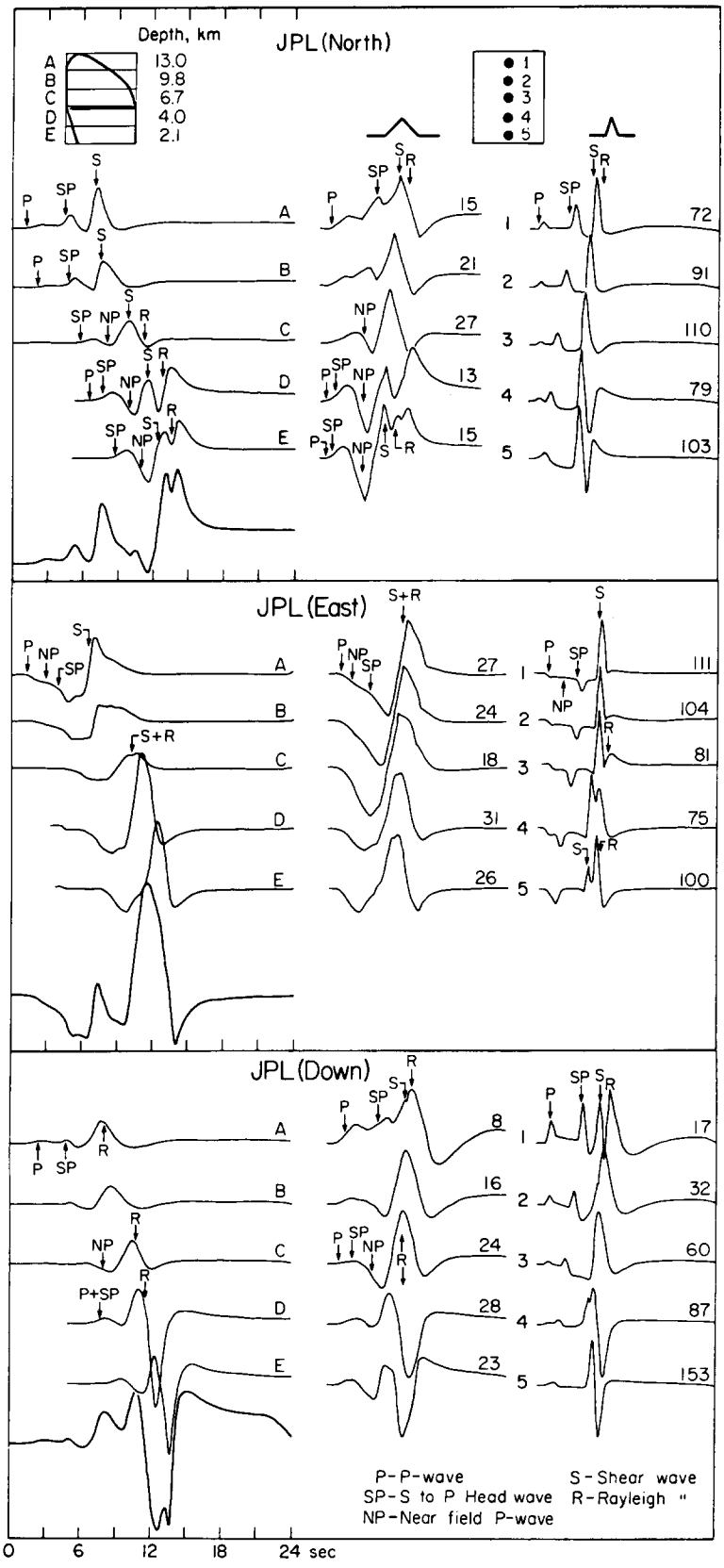

FIG. 11. Decomposition of the synthetic ground motions for JPL and the model Norma 170. See Figure 10 for a more detailed explanation.

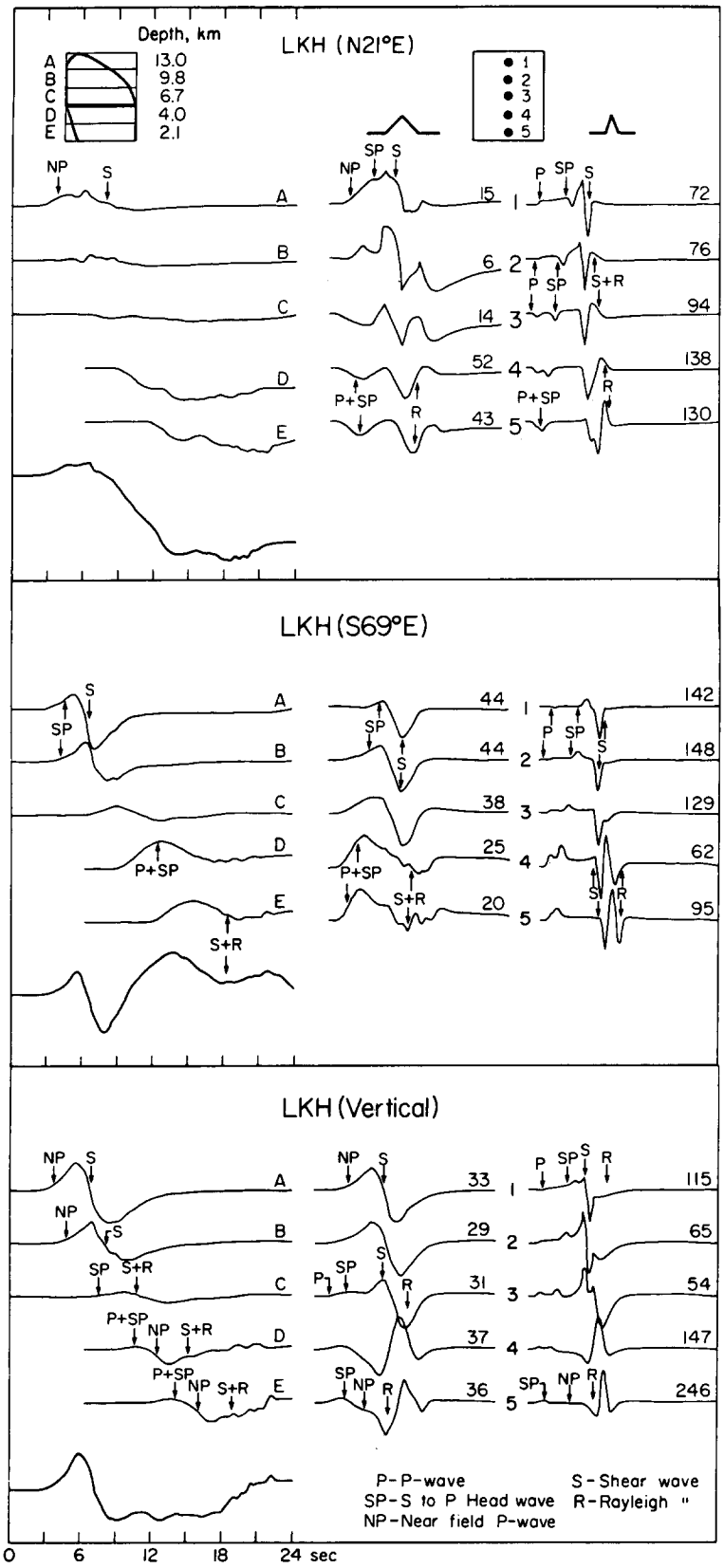

FIG. 12. Decomposition of the synthetic ground motions for LKH and the model Norma 170. See Figure 10 for a more detailed explanation.

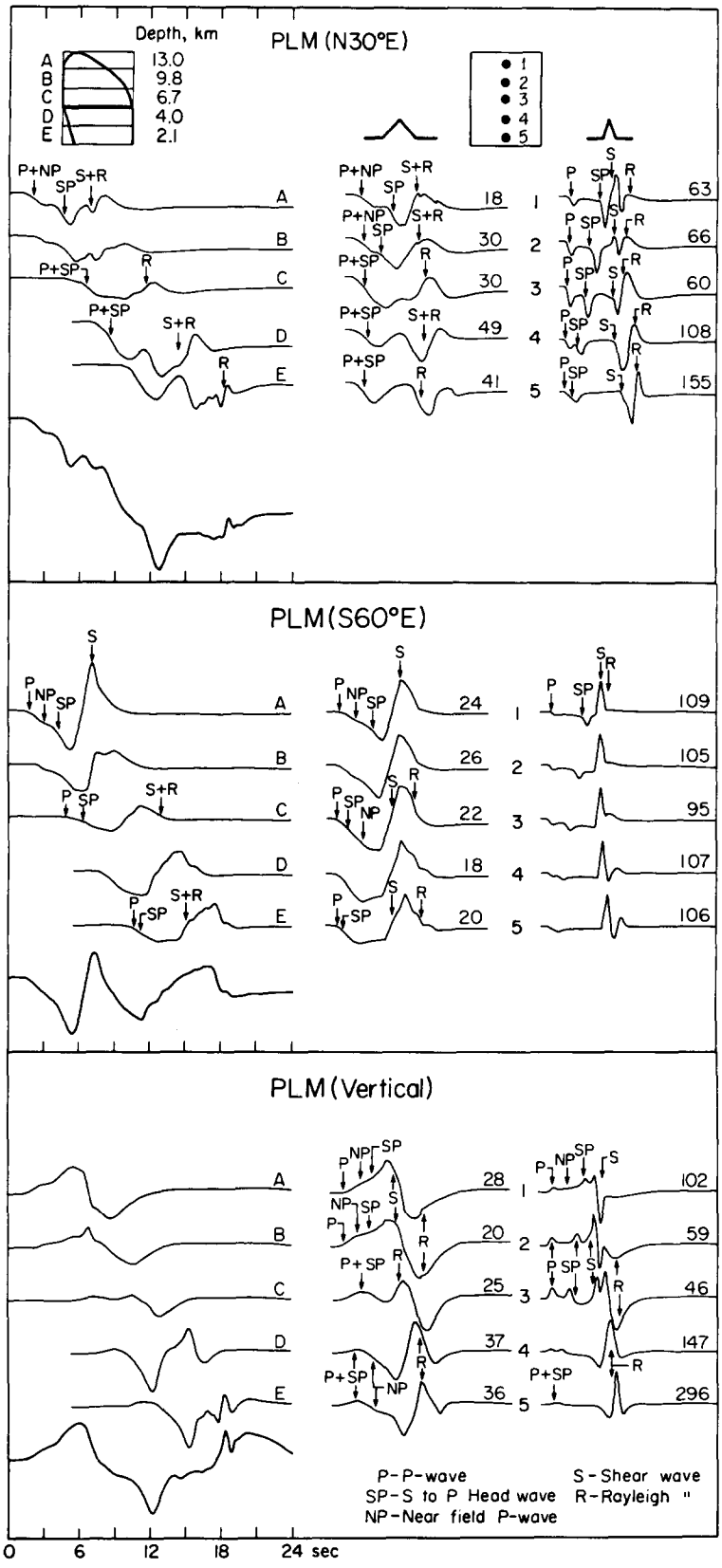

FIG. 13. Decomposition of the synthetic ground motions for PLM and the model Norma 170. See Figure 10 for a more detailed explanation.

Let us begin by studying the response of the lower fault. We have already pointed out that a major problem is the relative amplitudes of the first pulses seen at PAC and LKH. We can see that the first pulse at PAC consists of a near-field P wave which is followed immediately by the far-field shear wave. At LKH, this pulse is formed by the positive interference of the S to P head wave and the near-field P wave. They are directly followed by a postcritical angle shear wave (for a better discussion of the nature of these arrivals, see Heaton, 1978). Now look at the vertical responses for the deepest point source for the stations PAC and LKH. The ratio of the amplitudes of the vertical components of the PAC and LKH point responses is on the order of 2:1. Now notice that the ratio of the amplitudes of the first vertical pulse that was observed at PAC and LKH was on the order of 20:1! Clearly, there will be trouble explaining this pulse with a deep point source. This observation is crucial to the construction of our later models in which we optimize directivity effects for PAC and LKH.

An interesting consequence of our preceding discussion is that we have discovered a way to easily add high-frequency pulses to northern station records without seriously affecting the synthetics for the southern stations. We can incorporate several short duration events into our model. If these extra events had a moment of only 10^{25} ergs, they could cause visible short duration pulses on the northern stations. Actually the motions observed at LKH are so small and long period, that we suspect that the rupture is fairly coherent.

We will now examine the upper section of the fault in more detail. Since PAC lies only 2.5 km above the fault plane, it is very sensitive to the time history of this upper plane. It is easy to see that the near-field terms, or more specifically, the static parts of the solution, are beginning to dominate over the far-field terms. Particularly large static displacements occur on the vertical component. If we look back to Figure 9, then we see that this large vertical offset cannot be seen in the observed records. We can also see that it would be nice if we could produce a similar pulse on the north component of motion. By carefully studying many point responses as well as static solutions for finite faults in a homogeneous half-space (Mansinha and Smylie, 1971), we were able to deduce that as the rupture proceeds toward and just beneath PAC, large static vertical displacements will inevitably occur. Obviously, the way to alleviate the problem of large vertical displacements at PAC is to require that the fault offsets are small for those parts of the fault which are beneath PAC. If the faulting is small beneath PAC, then where does the moment of the upper fault come from? By studying the static solutions, we discover that large displacements to the south would be observed at PAC if there was significant faulting on the very shallowest parts of the fault. Conveniently, a large offset to the south will help explain the north component of motion observed at PAC.

We have studied the inadequacies of Norma 170 and have decided that the following features should have been included: (1) greater directivity on the lower fault to explain the beginning pulses seen at LKH and PAC; (2) small fault offsets beneath PAC to explain the vertical record at PAC; (3) large fault offsets south of PAC to explain the north component of PAC.

In Figure 14 we show a model, Norma 163, which incorporates the features which we have just mentioned. The source parameters for this model are summarized in Table 1. The comparisons of observed and synthetic records are also shown in Figure 14. Clearly Norma 163 fits the records much better than our previous models. This is no accident, since in reality, we tested many other models before arriving at

Norma 163. This is not to say that Norma 163 is the best half-space model possible, but it is the best we found before tiring of the game.

There are many details included in Norma 163 and some of these are rather arbitrarily chosen. We will, however, try to justify certain features of this model. Let

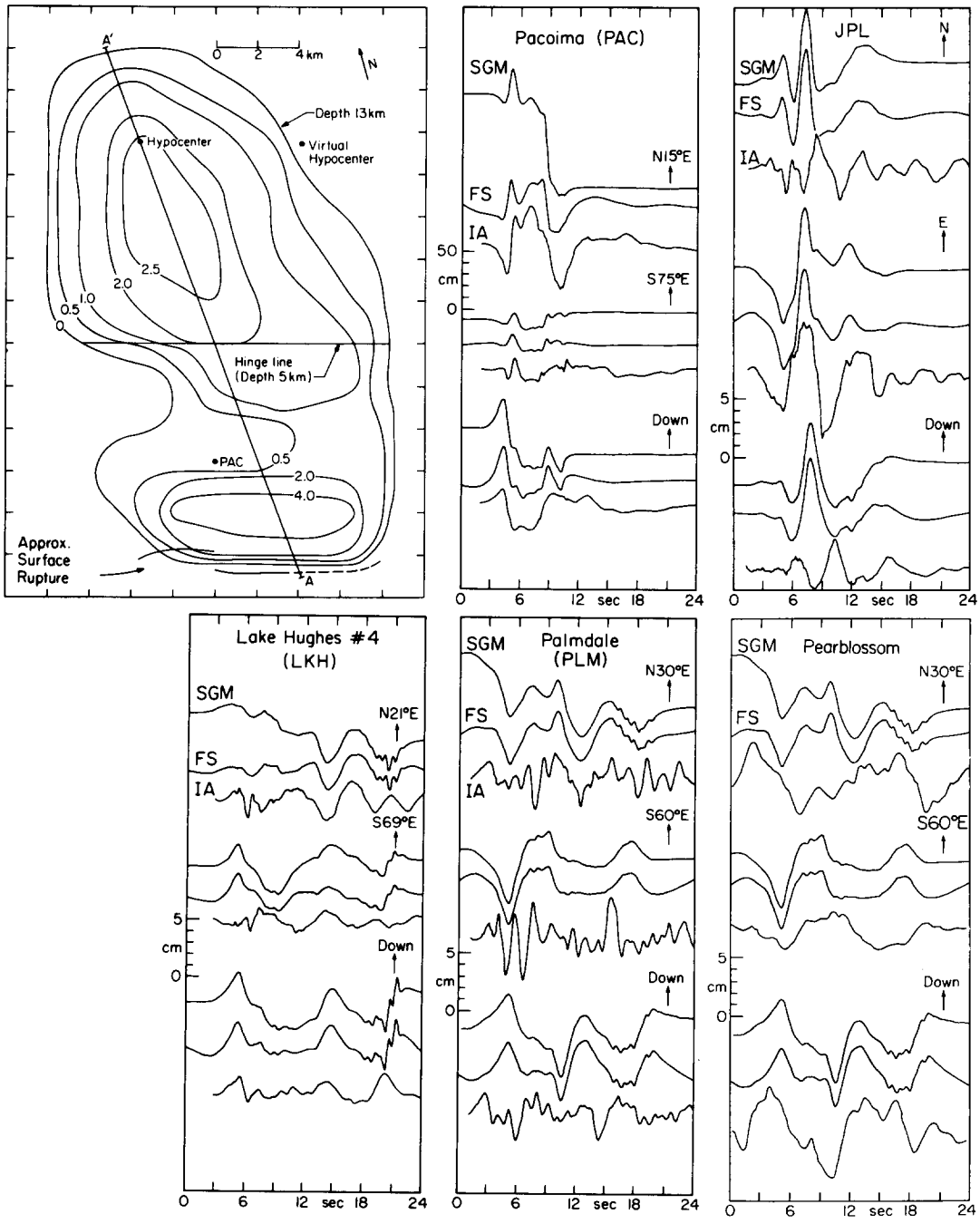

FIG. 14. Summary of the model Norma 163. The details of the rupture process are described in Table 1. See Figure 8 for explanation of SGM, FS, and IA. A comparison of the PLM synthetics with the observed Pearblossom (F103) displacements has been included.

us begin by examining the lower fault for Norma 163. We have increased the rupture velocity to 2.8 km/sec. There are several reasons for doing this. It substantially increases the amplitude of the shear wave at PAC without increasing the amplitude at LKH; that is, it enhances directivity. It also allows the timing of arrivals from the upper fault at PAC to be compatible with a hypocentral depth of 13 km. Notice that the hypocenter is almost due north of Pacoima and that the faulting seems to be skewed with respect to a line directly down the dip. This has two effects. The first is to produce the beginning pulse seen on the S75°E record of PAC. This pulse disappears when the faulting is aligned directly down the dip. The polarity of this pulse is reversed if the faulting is skewed to the east of the down-dip direction. A second effect is that directivity decreases the amplitude of the first pulse seen at LKH.

TABLE 1

SOURCE PARAMETERS FOR NORMA 163

	Lower Segment	Upper Segment
Depth of hinge (km)	5.0	
Strike	−75°	−75°
Dip	53°	29°
Rake	76°	90°
Rupture velocity (km/sec)	2.8	1.8
Rise time (sec)	0.8	0.8
Moment ($\times 10^{26}$ ergs)	0.8	0.6
Hypocentral longitude	118.41°E	118.33°E
Hypocentral latitude	34.44°N	34.42°N
Hypocentral depth (km)	13.	13.

The faulting in Norma 163 is predominantly unilateral upward and this, again, is to optimize directivity effects. We will delay a closer look at this particular problem until a little later. Notice that the 2-m contour in Figure 14 is elongated toward PAC. Again, this increases directivity effects. If the fault width is increased significantly, then the ratio of LKH to PAC amplitudes quickly decays. We are pleasantly surprised to discover that this ratio can help constrain the horizontal dimensions of faulting.

Details used on the upper fault plane are based mostly on an analysis of the PAC records. The hypocenter for the upper fault is equidistant from the hypocenter on the lower fault, but it has been shifted eastward. Thus the direction of rupture propagation changes from a southerly to a south-southwesterly direction at the hinge line. This is a detail which improves the comparison of the synthetic and observed S75°E records. Although we used a 0.8 sec rise time throughout the fault, it would appear that a slower rise time for the upper part of the fault would be more appropriate as can be seen on the N15°E PAC record. That is, it appears that the southward displacement at PAC occurs too quickly. This situation could be alleviated by a longer rise time (about 2 sec) or perhaps a slower or less coherent rupture process.

At stations other than PAC, the largest arrival from the upper fault is a Rayleigh wave. Our Rayleigh velocity is the half-space Rayleigh velocity which is probably significantly higher than the Rayleigh velocity for the real earth which has lower velocities near the surface. We have included a 2-sec delay for all arrivals from the

upper fault for the three stations, JPL, LKH, and PLM. Although this appears to be an unsatisfactory way to model slower surficial seismic velocities, model experiments indicate that this approximation is reasonable at this stage of the source determination. We will discuss the effects of local structure at these stations as well as many others in a subsequent paper.

Notice that Norma 163 significantly improves the comparison between observed and synthetic records for later portions of the LKH records. This is due to the added character of the upper fault. The PLM records do not look much better than they did before, but we now suspect that the Palmdale observation may be seriously affected by local site conditions. Our suspicions are based on the distinct 1 Hz ringing that occurs on the velocity components, especially the N30°E record as displayed in Figure 5. Furthermore, this station is sitting on substantial sedimentary cover which could easily produce such effects. And finally, the Pearblossom records do not show these short period pulses and this station is located on bedrock. We have included a comparison of the Pearblossom records with the synthetics appropriate for Palmdale. Pearblossom is at a slightly different azimuth and larger distance (see Figure 1). It appears that fitting Pearblossom instead of Palmdale would have been more useful for this study; however, the existing match is probably sufficient for our purposes.

In Figures 15 through 18 we show detailed interpretations of each of the synthetic records for the model, Norma 163. These figures are very similar to the previous set of Figures 10 through 13. Since the very top of the fault has become so important, we have included a sixth strip which shows the response of the shallowest section of the fault. As before, the middle row of responses shows point-source responses which are convolved with a 3-sec triangular far-field time function. Peak amplitudes (in centimeters) are shown for a moment of $\pi \times 10^{26}$ ergs. The right-hand column of responses contains far-field step function responses. They are very useful since they allow a positive identification of the various phases present. For the most part, these figures are self-explanatory. There are some features worth noting, though. If one looks back to Figure 2, then one can see that the large velocity pulse seen at PAC is the far-field shear wave from the bottom of the fault. This arrival has been greatly enhanced by directivity. Peak accelerations at PAC occurred at about the time that energy is arriving from our strong near-surface faulting. The large displacement pulse seen on the east component of JPL is comprised mainly of the direct S wave. Near-field P waves, S to P head waves, and Rayleigh waves are particularly important at the northern stations LKH and PLM.

Discussion

Now that we have constructed a model which seems to be compatible with the strong-motion data, we must attempt to evaluate its validity in light of other evidence. Specifically, Alewine's (1974) inversion of static vertical offset data provides us with an excellent test of the upper part of our model. He was able to fit the observed elevation changes with a high degree of accuracy. His model consisted of a three-dimensional fault in a half-space. Fault slip was allowed to vary with depth. Because of the nature of the static inverse problem, Alewine had excellent resolution on the top part of the fault, but the solution for the deeper parts was poorly constrained. Figure 19 shows plots of magnitude of fault slip versus distance along the profile A to A′ which is shown in Figure 14. These plots are for Alewine's inverse solution and for our solution, Norma 163. We believe that the most significant feature of this comparison is the 5-m fault offset which is included in both models for the shallowest part of the fault. Moreover, the offset as a function of depth

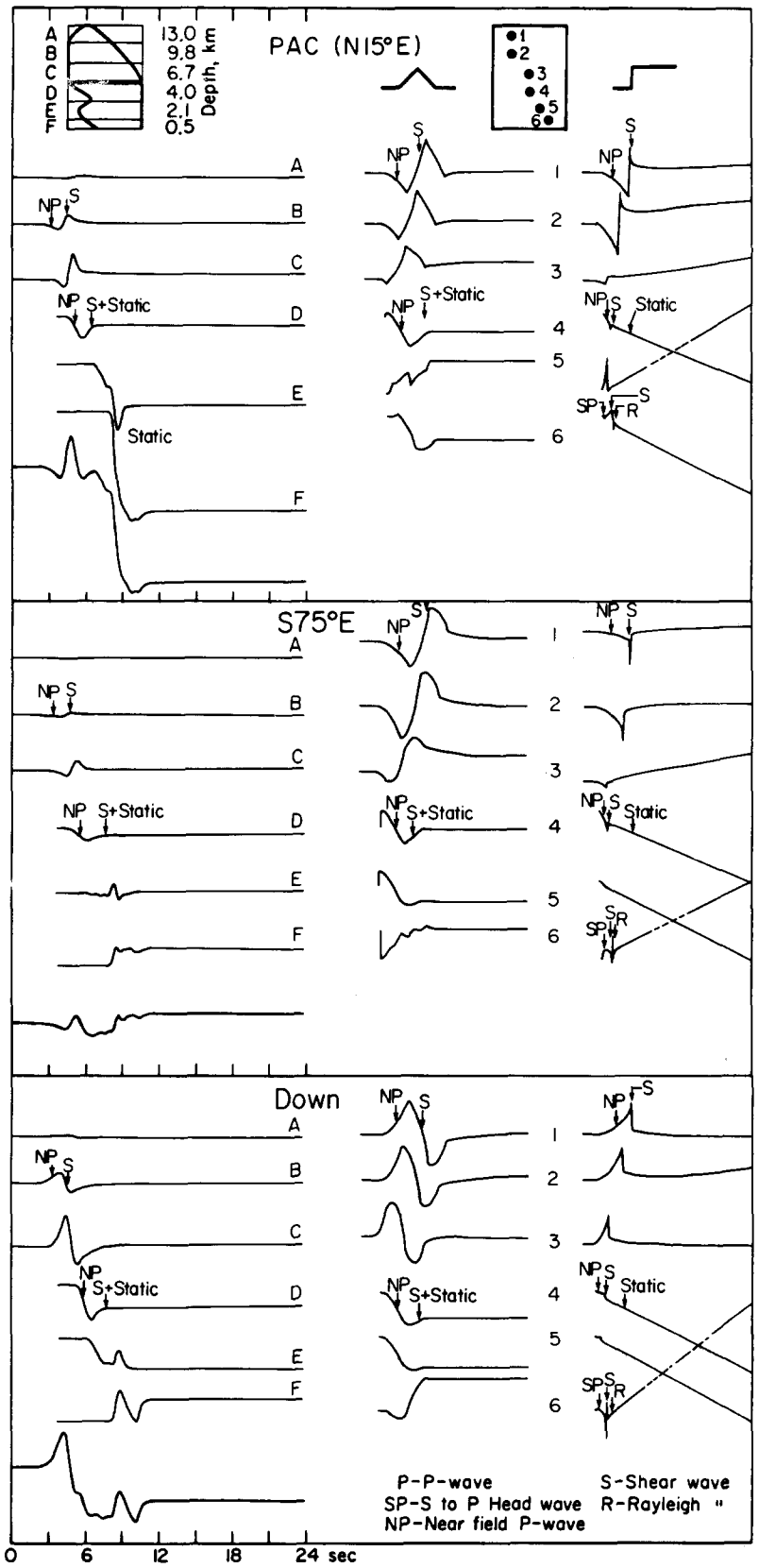

FIG. 15. Decomposition of the synthetic ground motions for PAC and the model Norma 163. The finite fault is broken into six strips whose individual contributions are shown on the *left*. Responses of point sources which lie in these strips have been convolved with 3-sec triangular far-field time functions and are displayed in the *middle* column. A moment of $\pi \times 10^{26}$ ergs was assumed and the corresponding amplitude is shown next to each trace. Far-field step-function responses for the same point sources are shown in the *right-hand* column.

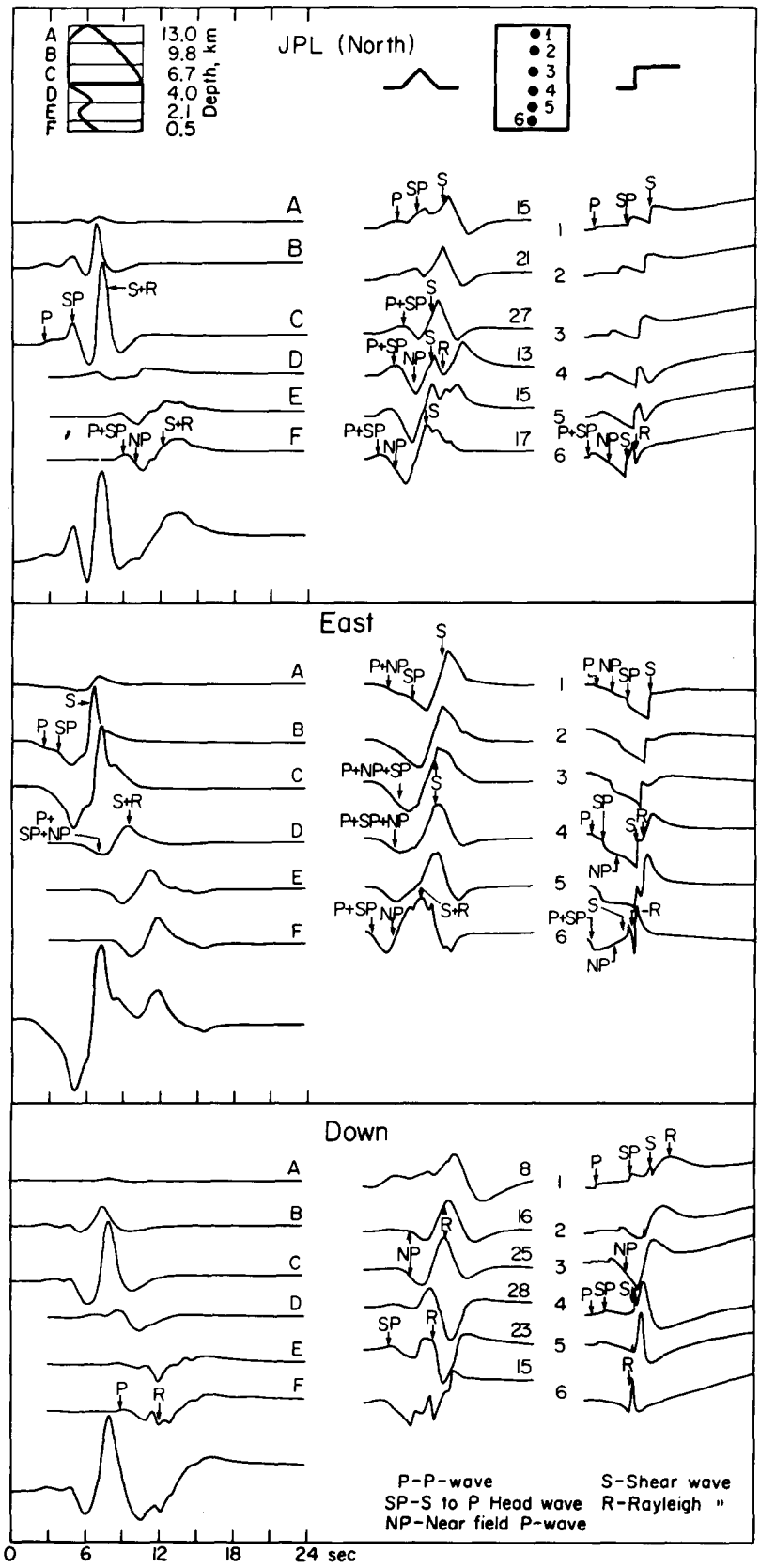

FIG. 16. Decomposition of the synthetic ground motions for JPL and the model Norma 163. See Figure 15 for a more detailed explanation.

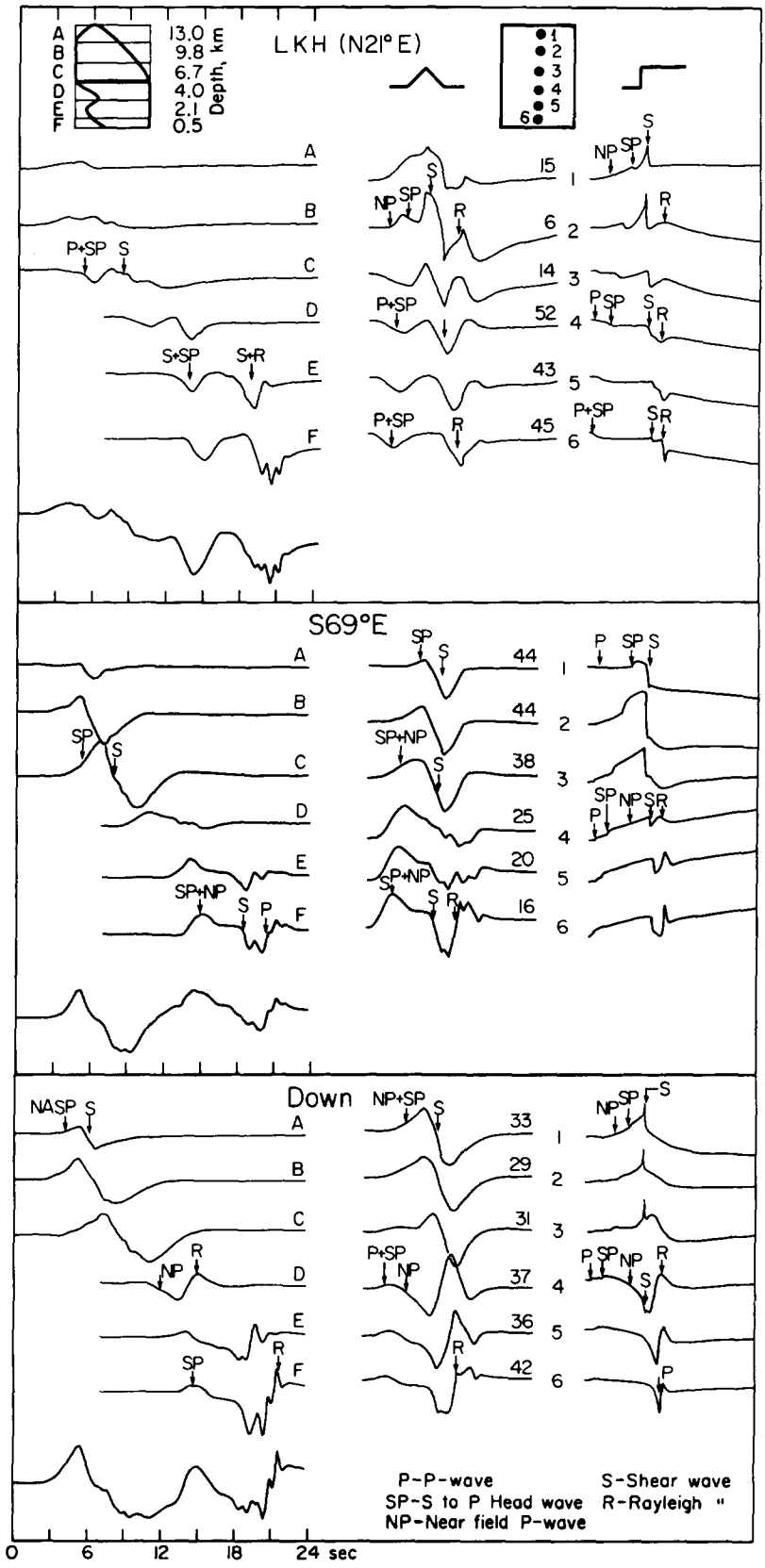

FIG. 17. Decomposition of the synthetic ground motions for LKH and the model Norma 163. See Figure 15 for a more detailed explanation.

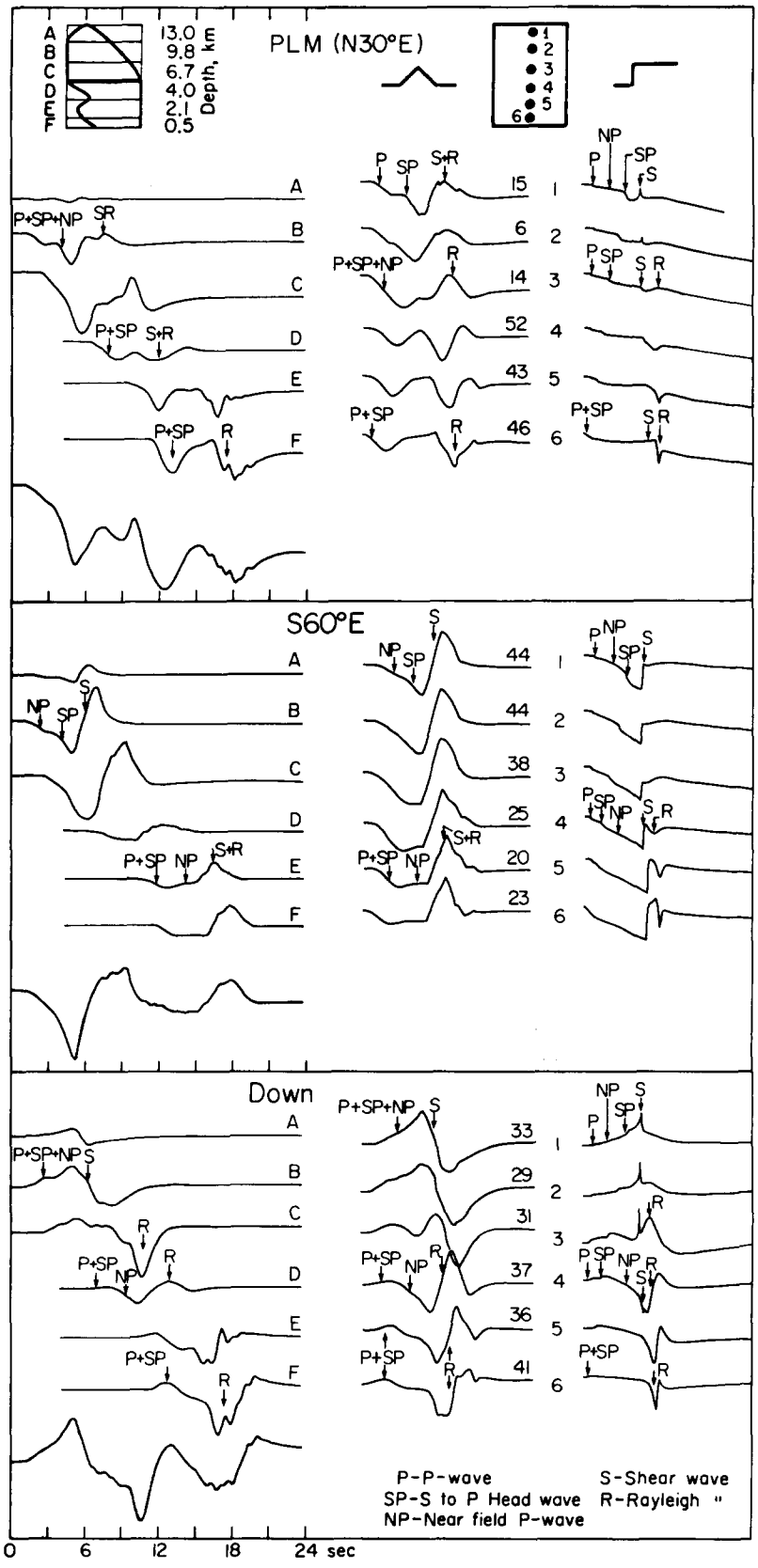

FIG. 18. Decomposition of the synthetic ground motions for PLM and the model Norma 163. See Figure 15 for a more detailed explanation.

decreases rapidly with both models. However, since Alewine's resolution for the deeper part of the fault is poor, it may be fortuitous that our two models produce similar displacements in the hypocentral region. Jungels and Frazier (1973) also studied the static vertical displacement data. They too concluded that large fault offsets were required on the very shallowest part of the fault. Because of the combined strong-motion and static displacement studies, we believe that the evidence for large shallow faulting is very strong.

Very intense shaking was observed in the area just north of the surface ruptures (Nason, 1973; Scott, 1973; Johnsen and Duke, 1973). This intense shaking occurred just above the section of the fault on which we believe the large offsets occurred. It seems likely that this is less than coincidental. Because of the particular geometry of this upper faulting, it is possible that areas within 1 km north of the surface

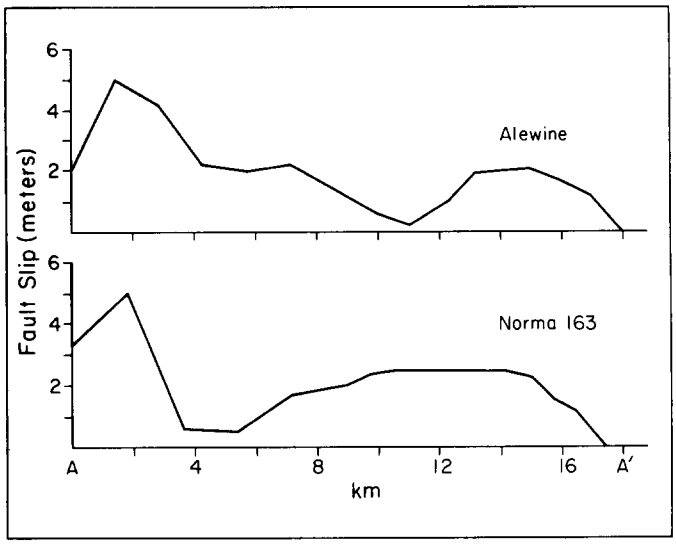

FIG. 19. Comparison of the fault slip as a function of distance along the line AA' of Figure 14. Alewine's (1974) model is from an inversion of static vertical uplift data. Notice that both the static offsets and this study seem to indicate massive faulting very near the free surface.

breaks experienced motions which were significantly different from those recorded at PAC.

The similarities between our model Norma 163 and Langston's (1978) models of teleseismic body waves are difficult to evaluate. We used the same fault geometry and focal mechanism. The relative timing of deep and shallow faulting seems to be roughly comparable. His calculated moment is 0.86×10^{26} ergs and ours is 1.4×10^{26} ergs. Perhaps the largest discrepancy between the models arises when considering directivity effects. Langston found that the teleseismic short-period direct P arrival was stronger than the pP arrival, even though these waves have roughly similar amplitudes at long periods. His interpretation is that the upward propagating rupture had a velocity of 1.8 km/sec. This low rupture velocity has the effect of depleting the upgoing phase, pP, of short-period energy. Langston also postulates that there is significant downward fault rupture which produces the short-period energy seen in the direct P phase. His modeling indicates that if one-fifth of the moment on the bottom fault were due to downward rupture at a velocity of 3.5 km/sec, then the correct ratio of short-period pP to P amplitudes would result. Here is the problem. We need strong, upward directivity to explain PAC. If there is strong, upward directivity, then how can we explain the depletion of short periods in pP?

Furthermore, Norma 163 is predominantly unilateral upward. Can our models accommodate significant downward rupture?

In the model, Norma 171, which is shown in Figure 20, we have put roughly one-fifth of our moment for the bottom fault beneath the hypocenter. All parameters are the same as for Norma 163 except that the moment on the bottom fault has grown to 10^{26} ergs. A larger moment was necessary to explain the amplitude of the first pulse seen at PAC. Comparisons between observed and synthetic records are also shown in Figure 20 for the stations PAC and LKH. The additional downgoing faulting has virtually no effect on the PAC synthetics. This downgoing faulting has, however, greatly increased the amplitude of the shear wave seen at LKH. The effect of downward faulting is to increase amplitudes for northern stations. This is an

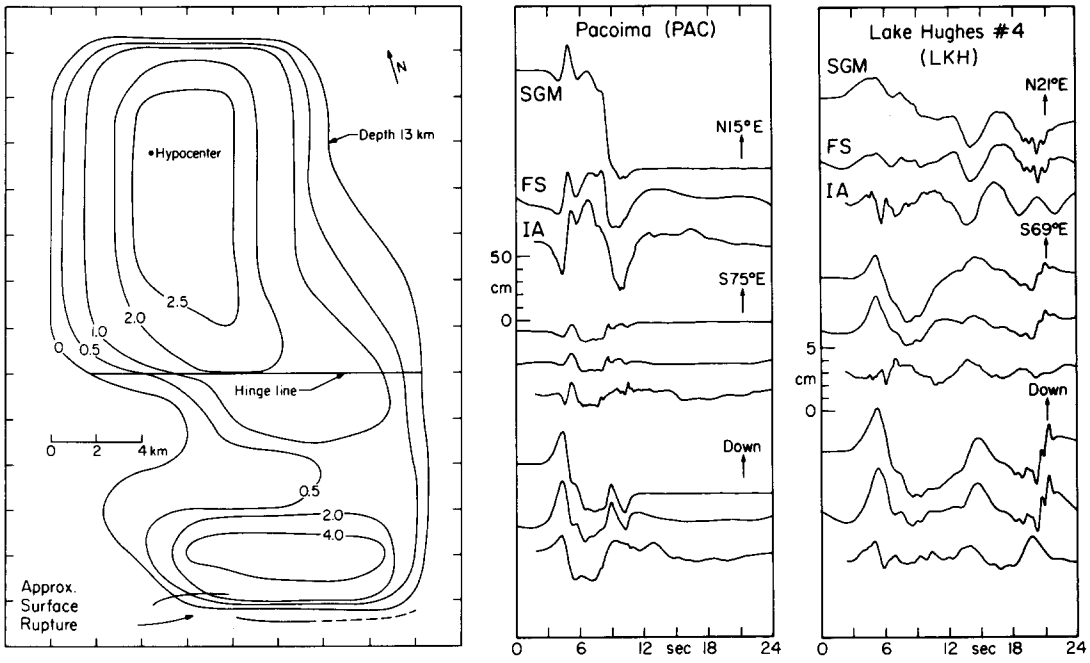

FIG. 20. Summary of the model Norma 171. The rupture parameters are given in Table 1. This model is similar to the preferred model Norma 163, but now the faulting is bilateral to test the suggested model of Langston (1978).

undesirable characteristic. Although we believe that our modeling is not sufficiently accurate to allow us to exclude the possibility of downward faulting, we can conclude that there seems to be no evidence for this downward rupture in the strong motion data. For the present, the explanation of the short-period teleseismic *P*-wave forms remains hidden.

In many respects, our model is very close to Trifunac's (1974) San Fernando model which was obtained by a linear inverse technique. Using a homogeneous whole-space model, Trifunac synthesized displacement records for PAC, LKH, and PLM. Only his PAC synthetics, though, are similar to ours. This should come as no surprise since we have already seen the importance of the free surface for the recordings at JPL, LKH, and PLM. Even for PAC, we were uncertain about whether a whole-space model could adequately approximate a half-space model. It is commonly assumed that the whole-space solution need only be doubled in order to approximate the response of a near-vertically incident wave on a free surface. As we often do, we allowed our physical intuition to play some tricks on us. We could

easily imagine that a wave which dynamically reflects at a free surface could cause twice the motion as that same wave in a whole space. But what about the static part? Should it also be doubled? Should half-space static displacements be twice as large as whole-space displacements given the same fault offset? Our initial reaction was that the whole-space and half-space answers should not differ by a factor of 2. PAC is so close to the fault that it might as well be on the fault. If we specify a certain dislocation, who cares whether we are on a half-space or in a whole-space? As you have probably already suspected, you are being baited. In certain instances, the half-space static solution is indeed almost twice the whole-space solution. In the case of the half-space, the upthrown block on which PAC rests experiences almost all of the static offset, whereas the downthrown block is hardly downthrown at all. In the whole-space solution, the upthrown and downthrown blocks move equally. Thus a factor of about 2 is present for the half-space to whole-space comparison for a station directly above a shallow angle thrust. A more complete description of this approximation is given by Boore and Zoback (1974).

The above discussion makes it easier to understand why Trifunac's (1974) and our models are similar. Although the free surface may be important for short-period arrivals from the very shallowest parts of the fault, displacements at PAC are most affected by the quasi-static offset of the upper fault. Trifunac's whole-space model seems to approximate the half-space reasonably well. However, we would urge that each case be examined carefully before deciding the appropriateness of this approximation.

Conclusions

So, where are we? We are probably somewhere in between. We feel that certain gross features of the faulting process can be resolved, but by no means have we fit the records perfectly. Feigning innocence, we have ignored the effects of topography and geological structure. Furthermore, we probably have not even found the best half-space model. However, we feel that we can draw some rather important conclusions from our naive study.

Directivity seems to play a major role in the observed motions. Predominantly unilateral faulting originated north of PAC at a depth of 13 km. The rupturing progressed smoothly over a fault with a width of about 6 km and displacements in the hypocentral region were about 2 m. The rupture velocity was near 2.8 km/sec for the deeper faulting and 1.8 km/sec for the shallow faulting. Fault offsets beneath PAC are very small. Massive faulting with fault offsets of 5 m occurred within several kilometers of the surface rupture. The large velocity pulse at PAC is a far-field shear wave which is enhanced by directivity. Peak accelerations at PAC are probably associated with the large shallow faulting.

Acknowledgment

We wish to thank Hiroo Kanamori, Paul Jennings, and James Brune for critically reviewing the manuscript. We also wish to thank Charles Langston and Thomas Hanks for useful discussions. Also Gladys Engen helped with the tedious computations. The figures were drafted by Laszlo Lenches and Joseph Galvan. This research was funded by the National Science Foundation (ENV76-10506, ENV76-21652, and EAR76-06619).

References

Alewine, R. W., III (1974). Application of linear inversion theory toward the estimation of seismic source parameters, *Ph.D. Thesis*, California Institute of Technology, Pasadena, 303 pp.

Allen, C. R., T. C. Hanks, J. H. Whitcomb (1973). San Fernando earthquake: Seismological studies and their implications, in *San Fernando California, Earthquake of February 9, 1971, vol. I, Geological and Geophysical Studies*, U.S. Government Printing Office, Washington, D.C.

Boore, D. M. and M. D. Zoback (1974). Near-field motions from kinematic models of propagating faults, *Bull. Seism. Soc. Am.* **64,** 321–342.

Hadley, D. and H. Kanamori (1978). Recent seismicity in the San Fernando region and tectonics in the west-central transverse ranges, California, (submitted for publication).

Hanks, T. C. (1974). The faulting mechanism of the San Fernando earthquake, *J. Geophys. Res.* **79,** 1215–1228.

Hanks, T. C. (1975). Strong ground motion of the San Fernando California earthquake: Ground displacements, *Bull. Seism. Soc. Am.* **65,** 193–225.

Hartzell, S. H., G. A. Frazier, and J. N. Brune (1978). Earthquake modeling in a homogeneous half-space, *Bull. Seism. Soc. Am.* **68,** 301–316.

Heaton, T. H. (1978). Generalized ray models of strong ground motion, *Ph.D. Thesis,* California Institute of Technology, Pasadena, 292 pp.

Heaton, T. H. and D. V. Helmberger (1977). A study of the strong ground motion of the Borrego Mountain, California, earthquake, *Bull. Seism. Soc. Am.* **67,** 315–330.

Heaton, T. H. and D. V. Helmberger (1978). Predictability of strong ground motion in the Imperial Valley: Modeling the M 4.9, November 4, 1976 Brawley earthquake, *Bull. Seism. Soc. Am.* **68,** 31–48.

Helmberger, D. V. and G. Harkrider (1978). Modeling earthquakes with generalized ray theory, in *Modern Problems in Elastic Wave Propagation,* J. Miklowitz and J. D. Achenbach, Editors, John Wiley and Sons, New York.

Hudson, D. E., A. G. Brady, M. D. Trifunac, and A. Vijayaraghavan (1971). Strong-motion earthquake accelerograms, corrected accelerograms and integrated velocity and displacement curves, vol. II, part A, Earthquake Eng. Res. Lab., *EERL 86–88,* California Institute of Technology, Pasadena.

Johnsen, K. E. and C. M. Duke (1973). Damage distribution in the Sylmar Valley area, in *San Fernando, California, Earthquake of February 9, 1971, vol. I, part B, Effects on Building Structures,* U.S. Government Printing Office, Washington, D.C.

Jungels, P. H. and G. A. Frazier (1973). Finite element analysis of the residual displacements for an earthquake rupture: Source parameters for the San Fernando earthquake, *J. Geophys. Res.* **78,** 5062–5083.

Langston, C. A. (1978). The February 9, 1971 San Fernando earthquake: A study of source finiteness in teleseismic body waves, *Bull. Seism. Soc. Am.* **68,** 1–29.

Mansinha, L. and D. E. Smylie (1971). The displacement fields of inclined faults, *Bull. Seism. Soc. Am.* **61,** 1433–1440.

Nason, R. (1973). Increased seismic shaking above a thrust fault, in *San Fernando, California, Earthquake of February 9, 1971, vol. I, part A, Geological and Geophysical Studies,* U.S. Government Printing Office, Washington, D.C.

Nigam, N. C. and P. C. Jennings (1968). *Digital Calculation of Response Sepctra from Strong-Motion Earthquake Records,* Report from the Earthquake Engineering Research Laboratory, California Institute of Technology, Pasadena, 65 pp.

Scott, N. H. (1973). Felt area and intensity of San Fernando earthquake, in *San Fernando, California, Earthquake of February 9, 1971, vol. I, part A, Geological and Geophysical Studies,* U.S. Government Printing Office, Washington, D.C.

Trifunac, M. D. (1971). Zero base-line correction of strong motion accelerograms, *Bull. Seism. Soc. Am.* **61,** 1201–1211.

Trifunac, M. D., F. E. Udwadia, and A. G. Brady (1973a). Analysis of errors in digitized strong-motion accelerograms, *Bull. Seism. Soc. Am.* **63,** 157–187.

Trifunac, M. D., A. G. Brady, and D. E. Hudson (1973b). Strong-motion earthquake accelerograms, corrected accelerograms and integrated ground velocity and displacement curves, vol. II, part C, G, J, Earthquake Eng. Res. Lab., *EERL 73–75,* California Institute of Technology, Pasadena.

Trifunac, M. D. (1974). A three dimensional dislocation model for the San Fernando, California, earthquake of February 9, 1971, *Bull. Seism. Soc. Am.* **64,** 149–172.

Wiggins, R. A., G. A. Frazier, J. Sweet, and R. J. Apsel (1978). Simulation of earthquake ground motions, in *Proceedings of N.S.F. Seminar-Workshop on Strong Ground Motion,* D. V. Helmberger and P. C. Jennings, Editors.

SEISMOLOGICAL LABORATORY
CALIFORNIA INSTITUTE OF TECHNOLOGY
PASADENA, CALIFORNIA 91125
CONTRIBUTION NO. 3182

Manuscript received December 15, 1978